

1 **Distribution and sea-to-air exchange of carbon monoxide in surface microlayer**
2 **and subsurface seawater in the eastern marginal seas of China**

3 Lin Yang ^{a, b}, Bin Yang ^a, Jing Zhang ^{b, c, *}, Anja Engel ^d, Gui-Peng Yang ^{b, c, *}

4 ^a *Jiangsu Key Laboratory of Marine Bioresources and Environment, Jiangsu Ocean University, Lianyungang,*
5 *222005, China*

6 ^b *Frontiers Science Center for Deep Ocean Multispheres and Earth System, and Key Laboratory of Marine*
7 *Chemistry Theory and Technology, Ministry of Education, Ocean University of China, Qingdao 266100, China*

8 ^c *Laboratory for Marine Ecology and Environmental Science, Qingdao National Laboratory for Marine Science*
9 *and Technology, Qingdao 266237, China*

10 ^d *GEOMAR Helmholtz Centre for Ocean Research, 24105 Kiel, Germany*

11 *Corresponding author:

12 *E-mail address: zhangjouc@ouc.edu.cn (J. Zhang); gpyang@mail.ouc.edu.cn (G.P.*
13 *Yang)*

14
15
16 **Keywords:** Carbon monoxide; Enrichment Factors; Surface microlayer; Sea-to-air
17 flux; Photoproduction; Bacterial consumption; Eastern marginal seas of China

18
19
* Corresponding authors. Key Laboratory of Marine Chemistry Theory and Technology, Ministry of Education, Ocean University of China, Qingdao 266100, China
E-mail addresses: zhangjouc@ouc.edu.cn (J. Zhang); gpyang@mail.ouc.edu.cn (G.P. Yang)

20 Abstract

21 Sea-surface microlayer (SML) is the boundary interface between the atmosphere and
22 ocean, exhibiting an enrichment of dissolved organic matter (DOM) and participating in sea-
23 to-air gas exchange. However, how DOM enrichment in the SML controls the flux of several
24 gases in sea-to-air exchange remains poorly understood. In our study, incubation
25 experiments and in-situ investigation in the eastern marginal seas of China were conducted
26 to determine the distribution of carbon monoxide (CO) and its production and consumption
27 rates in the SML during winter. Chromophoric DOM (CDOM) (92%) and fluorescent DOM
28 (FDOM) (92%) were frequently enriched in the SML during winter, and the enrichment of
29 CO was lower than the enrichments of CDOM and FDOM. CO ranged from 0.48 to 2.81
30 nmol L^{-1} ($1.22 \pm 0.85 \text{ nmol L}^{-1}$) and 0.50 to 3.61 nmol L^{-1} ($1.54 \pm 1.61 \text{ nmol L}^{-1}$) in the
31 subsurface layer (SSW) and the SML, respectively, with higher concentration observed in
32 the SML due to CDOM enrichment. Enrichment in the SML was expressed as enrichment
33 factors (EFs) defined as the ratio of values in the SML to those in the SSW. **Although CO,**
34 **CDOM and FDOM concentrations decreased from in-shore regions to open oceans, higher**
35 **enrichment factors (EFs > 2) of CO and CDOM and FDOM in the SML were generally**
36 **observed in the off-shore areas.** Considering the photoproduction rate (mean value: 12.41
37 $\text{nmol L}^{-1} \text{ d}^{-1}$) of CO in the SML was significantly higher than that in the SSW (10.32 nmol
38 $\text{L}^{-1} \text{ d}^{-1}$), the enrichment and the concentration of CO in the SML showed a diurnal variation,
39 with the higher values observed in the early afternoon. The flux of CO exhibited a
40 significantly negative correlation with the CDOM absorption coefficient at 254 nm and
41 marine-humic-like FDOM in the SML, suggesting that elevated DOM could stimulate the

42 photoproduction of CO, but may also decrease sea-to-air CO exchange in the SML. Given
43 the importance of the organic-rich SML as a diffusion layer in the air–sea exchange of
44 climate-relevant gases and heat, understanding the layer’s enrichment processes is crucial.

45 **1. Introduction**

46 Carbon monoxide (CO) is an indirect greenhouse gas, and it plays an important
47 role in atmospheric chemistry (Nguyen et al., 2020). It is the predominant sink of
48 hydroxyl radical (OH•, Conte et al., 2019; Cordero et al., 2019), which oxidizes
49 pollutants and greenhouse gases (such as CH₄) emitted to the atmosphere by human
50 activities (Nguyen et al., 2020). The photodegradation of dissolved organic matter
51 (DOM) is thought to be the main source of CO in the ocean (Stubbins et al., 2006), and
52 the ocean acts as a net source of atmospheric CO (Mopper and Kieber, 2002). In
53 addition, direct production of CO by phytoplankton has been observed in laboratory
54 experiments (Troxler et al., 1972; Gros et al., 2009) and dark/thermal production was
55 also inferred from modeling at Bermuda Atlantic Time Series (BATS, Kettle, 2005),
56 and from incubations of water samples from the Delaware Bay (Xie et al., 2005) and St
57 Lawrence estuary (Zhang et al., 2008). Microbial consumption and sea-to-air fluxes
58 (Doney et al., 1995; Song et al., 2015) of CO are considered the primary sinks of
59 oceanic CO (Zafiriou et al., 2003). The average annual sea-to-air flux accounted for 10%
60 of the global CO sinks estimated by Zafiriou et al. (2003), Conte et al. (2019) and Yang
61 et al. (2024). In the ocean, CO acts as a microbial energy source that supports food
62 webs, a link in carbon cycling that connects surface and deep waters, and a modulator

63 of oxygen cycles. With increasing concern about atmospheric pollution and the
64 potential role of CO₂, a primary goal of studying oceanic CO₂ concentrations is to
65 evaluate its long-term stability and distribution trends in the marine boundary layer
66 (Conte et al., 2019; Xu et al., 2023), where the ocean and atmosphere exchange
67 momentum, heat, moisture, and gases.

68 The ocean surface layer plays a vital role in climate change through the sea-to-air
69 exchange of greenhouse gases. The sea-surface microlayer (SML) is located at the sea-
70 to-air interface and is considered to play a critical role in global biogeochemical cycles
71 and climate change by regulating the sea-to-air exchange of gases and aerosol particles
72 (Liss and Duce, 1997; Cunliffe et al., 2013). In addition, SML is exposed to the most
73 intense solar radiation of any seawater layer, especially ultraviolet (UV) light, and
74 shows significantly higher colored dissolved organic matter (CDOM) concentration
75 and microbial abundances compared to the subsurface layer (SSW, Obernosterer et al.,
76 2006; Obernosterer et al., 2008; Wurl et al., 2009; Yang et al., 2022). For decades,
77 articles have emphasized the presence and enrichment of organic matter and gases (CO₂
78 and DMS) in the SML (Liss and Duce, 1997; Orellana et al., 2011; Ma and Yang, 2023;
79 Sugai et al., 2020), but it remains unclear how this is maintained whilst CO₂ is lost to
80 the atmosphere.

81 The role and response of the SML, along with the complex interplay of biological,
82 geochemical, and physical processes, govern the transfer of CO₂ from the SSW, where
83 it can either be consumed by bacteria or released into the atmosphere. Generally, the
84 sea-to-air flux is estimated from CO₂ concentration in sea surface waters (2 to 10 m),

85 but there is evidence that biogeochemical processes within the SML may also affect the
86 CO flux (Sugai et al., 2020). CDOM enrichment in the SML relative to the SSW has
87 been reported, with an enrichment factor (EF) range of 0.4 to 6.7 (Huang et al., 2015;
88 Shaharom et al., 2018; Yang et al., 2022), and mediates all mass transfer across the
89 SML (Rickard et al., 2019 and 2022). Although intense solar radiation and enrichment
90 of DOM may promote CO photoproduction involving SML (Cunliffe et al., 2013;
91 Pereira et al., 2018; Sugai et al., 2021), and likely modify sea-to-air gas transfer velocity
92 (k_w) of CO and other gases (Pereira et al., 2018). However, CO-related data from the
93 SML is especially scarce, and the fate of CO in the SML remains unknown, because of
94 the sampling limitation (Engel et al., 2017). Our study hypothesized that SML-specific
95 environmental changes (i.e., enrichment processes and biogeochemical processes) and
96 the abundance and composition of DOM in the eastern marginal seas of China influence
97 the rate of sea-to-air CO exchange, and they contribute to the formation of the marine
98 boundary layer involved in atmospheric chemistry and climate regulation.

99 **2. Materials and Methods**

100 *2.1 Study Area*

101 The Yellow Sea (YS) and the East China Sea (ECS) are marginal seas of the
102 western Pacific Ocean with complicated hydrological characteristics and are
103 substantially affected by the Yellow Sea Cold Water Mass (YSCWM), the Kuroshio
104 Current, and the coastal currents (Fig. 1). The YSCWM is a low-temperature ($< 10^\circ\text{C}$)
105 and high-salinity (32.0–33.0) water mass. Seawater in the Kuroshio presents high

106 temperatures (20–29°C), high salinities (34.2–34.8), and low suspended particulate
107 concentrations (SPC) ($< 2 \text{ mg L}^{-1}$) (Yang et al., 2022). The Changjiang River
108 contributed more than 80% of the total freshwater inflow to the YS and the ECS (Wang
109 et al., 2020). In addition, the atmospheric circulation in the study area was generally
110 governed by the East Asian monsoon, with strong northerly winds prevailing from
111 September to April. Low pressure over the northwestern Pacific Ocean produced
112 offshore winds that transported continental air masses into the study area (Li et al.,
113 2019). This interaction significantly influences the hydrological conditions, circulation
114 structures, material exchange, ecological environment, and the biogeochemical
115 processes of CO and DOM in the region (Chen, 2009; Yu et al., 2025; Zhang et al.,
116 2007).

117 *2.2 Sampling and analysis*

118 We collected 52 paired SML and SSW water samples in the YS and ECS aboard
119 the R/V “*Dong Fang Hong 3*” from 28 December 2019 to 16 January 2020. [There were](#)
120 [38 sampling stations during the daytime \(7: 00-19: 00\) and 32 sampling stations during](#)
121 [the nighttime \(19: 00-7: 00, Table S1\)](#). SSW samples were collected at 2–5 m depth
122 using $24 \times 10 \text{ L}$ Niskin bottles mounted on a rosette equipped with a conductivity–
123 temperature–depth (CTD) profiler. SML sampling used a Garrett Screen (Garrett, 1965;
124 Chen et al., 2016; Ma and Yang, 2023) (mesh: 16 mm, wire diameter: $0.36 \mu\text{m}$; effective
125 surface area: 2.025 cm^2) according to standard procedures (Pereira et al., 2016;
126 Sabbaghzadeh et al., 2017) when seawater conditions were calm. While SML integrity

127 is disrupted by a moving vessel, or when sampling from its stern (Cunliffe and Wurl,
128 2014; Wurl et al., 2016), the SML can be successfully sampled from a vessel's bow
129 while on-station (Sabbaghzadeh et al., 2017) with the ambient waterflow toward the
130 RV (Cunliffe and Wurl, 2014). The sampling distance is at a certain distance (5 ~ 8 m)
131 where the CTD sampler was deployed, and both SSW and SML CO did not change
132 during the sampling. We therefore adopted this procedure, hand-deploying the Garrett
133 Screen over the bow on the crest of a wave (Cunliffe and Wurl, 2014) and further
134 minimizing potential contamination (engines off, wheelhouse and afterdeck downwind)
135 (Pereira et al., 2016).

136 A TA3000R trace gas analyzer (Ametek, USA) was used to measure CO
137 concentrations in the atmosphere and seawater with a lower detection limit of 10 ppbv.
138 Before analysis, the instrument was calibrated using a CO standard gas (nominal
139 concentration: 100 ppbv in zero-grade air; analytical accuracy: $\pm 2\%$, State Center for
140 Standard Matter, China). The calibration was repeated every six hours during
141 measurements. Atmospheric CO samples ($[\text{CO}]_{\text{atm}}$, ppbv) were collected about 10 m
142 above sea level using a 10 mL gas-tight syringe (VICI, USA) and were obtained by
143 injecting atmospheric samples directly into the instrument through a PTFE hydrophobic
144 filter membrane (Millipore, USA, atmospheric CO samples were filtered for
145 dust/aerosol particles) into the TA3000R trace gas analyzer for determination. To
146 minimize the influence of ship emissions, $[\text{CO}]_{\text{atm}}$ samples were collected from the
147 highest deck of the ship (~10 m), facing the wind, with 8 mL gastight glass syringes
148 when the ship was decelerating. CO in seawater was measured using the headspace

149 equilibrium method (Xie et al., 2002), wherein a 50 mL sample bottle was filled with
150 seawater sample and sealed (as above), and then an equivalent amount of the seawater
151 sample was replaced with 8 mL of ultrahigh-purity N₂ using a gas-tight syringe. The
152 samples were then shaken at 300 r min⁻¹ for 5 min to ensure that the nitrogen-filled
153 headspace in the bottle reached gas-liquid equilibrium before 6 mL of the equilibrated
154 gas was extracted using a gas-tight syringe and injected through a PTFE hydrophobic
155 filter membrane (Millipore, USA) into the TA3000R trace gas analyzer for
156 determination (the PTFE filter membranes were set up to prevent the potential entry of
157 liquid water). The measured equilibrated headspace mixing ratio of CO (ppbv) was
158 corrected using the saturated water vapor pressure and standard atmospheric pressure
159 (Stubbins et al., 2006) and then converted to obtain the concentration of dissolved CO
160 (nmol L⁻¹) in seawater. The method's lower detection limit was 0.02 nmol L⁻¹, with an
161 analytical accuracy of better than 10%.

162 CO data from the SML samples is scarce. The SML samples were collected in 500
163 mL brown sample bottles. The screen was held level and dipped into the sea surface,
164 moved laterally to sample from an undisturbed film, and then withdrawn slowly from
165 the surface. Repeated dipping (11 times, 600 mL) was conducted until the desired
166 volume was collected (the depths of the SML samples ranged within 100–500 μm,
167 Garrett, 1965). The screening method is often applied during field studies because of
168 its relative quickness and large sample volume compared to other techniques (Chen et
169 al., 2016). CO in seawater samples was collected and measured first on board,
170 immediately after collection. A comparison showed that screen-collected samples

171 usually exhibit greater microlayer enrichment of gas than the plate-collected samples,
172 indicating that the screen sampler might be more effective for in-situ measurements
173 (Yang et al., 2001). Although established sampling techniques of the SML (Garrett
174 screen and glass plate) are associated with high losses for the volatile trace gases (Engel
175 et al., 2017). As the Garrett screen is widely used and can collect a large number of
176 SML samples in the short term (Turner and Liss, 1985; Walker et al., 2016; Yang et al.,
177 2001), we chose the Garrett screen.

178 CDOM, DOC, and Chl-*a* samples were filtered using 0.7 μm glass fiber filters
179 (GF/F, Whatmann) and the filtrates were transferred to 60- and 40-mL brown glass
180 bottles (pre-cleaned and pre-combusted) for later CDOM and DOC analyses. All
181 samples were frozen (-20°C) and protected from light. Upon arriving at the land
182 laboratory, samples were analyzed as soon as possible. Sea-surface temperature and
183 salinity were obtained from the sensors on the Seabird 911 CTD rosette. Seawater
184 temperature and salinity in the SML were measured *in situ* using a pre-calibrated multi-
185 parameter water quality probe (AP-5000, Aquaread Co., UK). Meteorological data (e.g.,
186 wind speed and air temperature, ~ 10 m) were recorded simultaneously by a ship-borne
187 weather instrument (Li et al., 2019, Table S1). Net solar radiation is the balance
188 between all incoming and outgoing radiant energy fluxes at the Earth's surface. Our
189 ocean surface net solar radiation was measured and recorded using a net radiometer
190 (Table S1). Ocean surface net solar radiation is significant in research on the Earth's
191 heat balance systems, sea-to-air interactions, and other applications.

192 *2.3 Photoexposure experiments*

193 The in-situ natural sunlight incubation experiment was conducted to estimate the
194 CO photoproduction rates in different seawater layers. SSW and SML samples for
195 photochemical incubation were collected from stations B1 and C4, as well as E2, FJ5,
196 P1, and P7, located in the YS and the ECS, respectively (Fig. 1). SML and SSW (5 m
197 below seawater surface) samples (SSW: 2 L; SML: 500 mL) were passed through a
198 0.22 μm PES filters (Pall Corp. Port Washington, NY, USA) immediately to remove
199 the majority of the bacteria and was then placed in an acid-washed and pre-combusted
200 quartz tubes (120 mL, acid-washed and pre-combusted) in a natural sunlight incubation
201 and sealed without headspace or air bubbles. Photo incubation experiments were
202 conducted on the ship immediately after sample collection. To measure the
203 photoproduction at solar radiation production rates of CO, the quartz tubes were treated
204 as follows: (1) uncovered quartz tubes exposed to full-spectrum irradiation; (2) quartz
205 tubes wrapped in multiple layers of aluminum foil to eliminate all light transmission.
206 Treatment (2) was subtracted from light-exposed treatments to remove the fraction of
207 CO produced by dark production. The quartz tubes were positioned under the in-situ
208 irradiation source to maximize the exposure of the sample; the water depth in each tube
209 was 5 cm (i.e., the diameter of the tube). SML and SSW quartz tubes were irradiated
210 for 4 hours and were exposed to direct solar irradiation while being held in a water bath
211 with circulating seawater. The change in the CO photoproduction with time can be seen
212 as a constant due to the relatively small amount of total radiation during the short
213 exposure time.

214 2.4 Microbial consumption and dark production experiments

215 Six stations were selected to determine the microbial consumption rates of CO
216 (YS: stations A1, B1, and C4; ECS: stations E2, T2, and S6). CO concentrations in
217 seawater samples were measured immediately after collection from the SSW and the
218 SML and used as background values. Seawater was used to fill 1 L glass syringes
219 equipped with a 3-way nylon valve, which were pre-cleaned with 10% HCl-Milli-Q
220 water and Milli-Q water until free of headspace, and wrapped with aluminum foil. The
221 syringes were immersed in a shallow tank of flowing water that was continuously
222 pumped from the sea to maintain the temperature of the incubation experiments equal
223 to that of the ambient surface seawater. Each sampling series consisted of 4–5 points,
224 and the data from each series were fitted exponentially to determine the consumption
225 rate constant (k_{bio}). The turnover time of the photochemical production (τ_{prod}) and
226 biological consumption (τ_{cons}) in the SML (SSW) was calculated by the following
227 equations (Doney et al., 1995; Jones and Amador, 1993):

$$228 \quad \tau_{\text{prod}} = [\text{CO}] \text{ in SML} / \text{photochemical CO production rate in SML} \quad (1)$$

$$229 \quad \tau_{\text{cons}} = [\text{CO}] \text{ in SML} / k_{\text{bio}} \text{ in SML} \quad (2)$$

230 The dark production incubations were used to eliminate the effect of dark
231 production from the microbial CO consumption measurements. According to Zhang et
232 al. (2008), the dark production is the abiotic dark production. Seawater was first filtered
233 through 0.2 μm polyethersulfone membranes and bubbled with CO-free gas (ultrahigh-
234 purity N_2 , China) to reduce the background CO values before being put into the 1 L
235 syringes as previously described. Then syringes were rinsed with the sample water and

236 then overflowed with the sample twice their volumes before they were closed without
237 headspace. All incubations were conducted in duplicate, and wrapped in multiple layers
238 of aluminum foil, and placed in the same incubator environment. Samples were
239 collected at 0, 0.5, 1, 2, and 4 h during incubation. CO incubation experiment was
240 performed under the same conditions as the CO degradation processes according to the
241 method of Xie et al. (2005) and Xu et al. (2023).

242 *2.5 Calculation of sea-to-air flux of CO*

243 The two-layer model proposed by Liss and Merlivat (1986) was used to calculate
244 the instantaneous sea-to-air flux of CO according to the following equation:

$$245 \quad F = k([\text{CO}]_{\text{surf}} - [\text{CO}]_{\text{eq}}) \quad (3)$$

246 Where F refers to the sea-to-air flux of CO ($\text{nmol m}^{-2} \text{h}^{-1}$), and k is the gas transfer
247 coefficient (cm h^{-1}) as a function of wind speed u (m s^{-1}) and the Schmidt number of
248 CO (Sc). In this paper, we used empirical formula E2011 (Edson et al., 2011), which
249 applies to wind speeds from 0 to 18 m s^{-1} (Wind speed ranged from 0.68 m s^{-1} to 12.00
250 m s^{-1}), to calculate the gas transfer coefficient as follows:

$$251 \quad k = (0.029u^3 + 5.4) (\text{Sc}/660)^{-1/2} \quad (4)$$

252 The Schmidt number of CO was referenced from the research of Zafiriou et al.
253 (2008):

$$254 \quad \text{Sc} = -0.0553t^3 + 4.3825t^2 - 140.07t + 2134 \quad (5)$$

255 where t is seawater temperature ($^{\circ}\text{C}$).

256 $[\text{CO}]_{\text{surf}}$ represents the concentration of CO in the initial SML and SSW seawater, calculated
257 by the following equation:

$$258 \quad [\text{CO}]_{\text{surf}} = pm_a (\beta p V_w + V_a) / (RT V_w) \quad (6)$$

259 Where P is the standard atmosphere pressure (atm) and m_a represents the concentration
260 of CO in the headspace when the sample reaches equilibrium. β is the Bunsen solubility
261 coefficient which is dependent on salinity and temperature (Wiesenburg and Guinasso,
262 1979). V_w and V_a are the volumes of seawater and headspace in the sample bottle,
263 respectively. T is temperature (in Kelvin) and R is the gas constant with the value of
264 $0.08206 \text{ atm L (mol K)}^{-1}$.

265 The daily fluxes ($\mu\text{mol m}^{-2} \text{ d}^{-1}$) of CO in the YS and the ECS were calculated
266 using the method reported by Stubbins et al. (2006) and Yang et al. (2011), based on
267 the hourly flux ($\mu\text{mol m}^{-2} \text{ h}^{-1}$). These hourly fluxes were examined on the scale of
268 individual days by plotting hourly fluxes against the time of day. Days without full
269 coverage of diurnal variations were discarded, leaving 4 days of data in the final
270 analysis. The area under each daily curve was calculated (OriginPro 8.0) to give daily
271 CO emissions.

272 *2.6 Determination of CDOM absorption*

273 The Napierian absorption coefficients of CDOM ($a_{\text{CDOM}}(\lambda)$ (m^{-1})) were calculated
274 as follows:

$$275 \quad a_{\text{CDOM}}(\lambda) = 2.303 A_{\text{CDOM}}(\lambda) / L \quad (7)$$

276 Where $A_{\text{CDOM}}(\lambda)$ is the absorbance of the sample at wavelength λ ; and L is the cell
277 pathlength of the quartz cuvette in meters (0.1 m, Stedmon and Markager, 2003).
278 CDOM absorption $a_{\text{CDOM}}(254)$ is an effective proxy for dissolved organic carbon (DOC)
279 and chlorophyll-*a* (Chl-*a*) concentrations in the eastern marginal seas of China (Yang
280 et al., 2021).

281 The spectral slope of the absorption spectrum was obtained by nonlinear fitting of
282 the absorption coefficient according to the following equation (Stedmon and Markager,
283 2003):

$$284 \quad a_{\text{CDOM}}(\lambda) = a_{\text{CDOM}}(\lambda_0)\exp[-S(\lambda - \lambda_0)] + K \quad (8)$$

285 Where $a_{\text{CDOM}}(\lambda)$ and $a_{\text{CDOM}}(\lambda_0)$ are the Napierian absorption coefficients at
286 wavelengths λ and λ_0 ; λ_0 is the reference wavelength (440 nm); S is the spectral slope
287 of the absorption spectrum; and K represents the background parameters with CDOM
288 removed (Yang et al., 2022). The specific UV absorbance (SUVA_{254}) can be used to
289 measure aromaticity (Weishaar et al., 2003) and molecular weight (Chowdhury, 2013)
290 of DOM, with higher values generally indicative of higher aromaticity. SUVA_{254} is
291 calculated by dividing the absorbance at 254 nm by DOC. Detailed Chl-*a*, DOC,
292 fluorescence DOM (FDOM), dissolved oxygen (DO), and wavelength (λ)-dependent
293 absorption coefficients of CDOM ($a_{\text{CDOM}}(\lambda)$) were determined in the laboratory using
294 published techniques. See supplementary information (Section S1) for analytical details.

295 2.7 Statistical analyses

296 The correlation coefficient (r) and probability (p) values were used to assess the
297 goodness of fit. The correlation matrix, analysis of variance, and principal components
298 analysis were performed with SPSS version 18.0 (SPSS Inc., Chicago, IL, USA) to
299 examine potential relationships between CO, DOM parameters, and environmental
300 factors. P values < 0.05 were considered significant. Shapiro-Wilk tests (Table S2,
301 supplementary information) indicated that the data were normally distributed for DOC
302 in the SSW ($p = 0.258$), but not for $[CO]_{SSW}$, $[CO]_{SML}$, $a_{CDOM}(254)$ in the SSW and
303 SML, and DOC in the SML ($p < 0.001$ for all). Therefore, all data were analyzed
304 consistently using non-parametric Kruskal-Wallis and Dunn-Bonferroni post-hoc tests.
305 Pearson's product-moment correlation was used to identify relationships between
306 parameters and was calculated at a 95% confidence level.

307 3. Results

308 3.1 Environmental Factors and CO Concentration in the SSW and the SML

309 Surface water temperature increased from 2.08°C at YS station H12 to 23.8°C at
310 ECS station E7 (mean value: $11.85 \pm 4.53^{\circ}\text{C}$, Fig. 2). Surface salinity increased from
311 28.85 at Changjiang River Estuary (CRE) station E1 to 34.62 at ECS station E7 (32.35
312 ± 1.17 , Fig. 2). Wind speed during sampling ranged from 0.68 m s^{-1} at station H9 to
313 12.00 m s^{-1} at station FJ1 ($6.09 \pm 2.50 \text{ m s}^{-1}$). The integrated net solar irradiance (14.09

314 $\pm 114.64 \text{ kW m}^{-2}$) during the in-situ incubation ranged from -111.8 kW m^{-2} at YS
315 station H5 to 417.9 kW m^{-2} at ECS station F4 (Table S1).

316 During the study period, $[\text{CO}]_{\text{SSW}}$ was particularly high at the station F4 (3.61
317 nmol L^{-1} , sampling time: 12: 43) in the SML and relatively high at the station P6 (2.81
318 nmol L^{-1} , sampling time: 14: 36) in the SSW (Fig. 2). The maximum $[\text{CO}]_{\text{SML}}$ was
319 observed during daytime, but the minimum $[\text{CO}]_{\text{SML}}$ was observed during nighttime
320 (station E2: 0.59 nmol L^{-1} , sampling time: 22: 22, Fig. 3). No significant difference was
321 observed between $[\text{CO}]$ in the SML (1.54 nmol L^{-1}) and the SSW (1.23 nmol L^{-1}) ($n =$
322 52 , $p = 0.11$, Wilcoxon signed-rank test). $[\text{CO}]$ mean value in the YS (SSW: $1.23 \pm$
323 0.40 nmol L^{-1} ; SML: $1.54 \pm 0.68 \text{ nmol L}^{-1}$) was similar to the concentration observed
324 in the ECS (SSW: $1.23 \pm 0.45 \text{ nmol L}^{-1}$; SML: $1.55 \pm 0.92 \text{ nmol L}^{-1}$) between the SML
325 and the SSW, respectively. $a_{\text{CDOM}(254)}$ in the YS (SSW: $3.59 \pm 0.89 \text{ m}^{-1}$; SML: $4.78 \pm$
326 0.85 m^{-1}) was higher than that in the ECS (SSW: $1.64 \pm 0.72 \text{ m}^{-1}$; SML: $4.70 \pm 3.35 \text{ m}^{-1}$)
327 in both the SML and the SSW. $a_{\text{CDOM}(254)}$ in the SML ($4.74 \pm 2.50 \text{ m}^{-1}$) showed
328 relatively higher values compared to the SSW ($2.52 \pm 1.26 \text{ m}^{-1}$) during winter. The
329 stronger negative linear relationship observed between salinity and $a_{\text{CDOM}(254)}$ was
330 observed in the SSW ($r = -0.716$, $n = 52$, $p < 0.01$), where the influence of terrestrial
331 input in this water layer was higher than that in the SML ($r = -0.038$, $n = 52$).

332 *3.2 Variations in parallel factor analysis (PARAFAC)-derived fluorescent DOM*
333 *components and factors controlling the composition of the fluorescent components*

334 The three fluorescent DOM components were determined statistically by
335 conducting Parallel factor analysis (PARAFAC) of the samples (Table S3; Fig. S1;
336 Supplementary Information 1.2). Component C1 was apparent with excitation and
337 emission peaks at 275 nm and 335 nm, respectively, and was likely a tryptophan-like
338 peak T (Yamashita et al., 2017). C2 exhibited excitation/emission (E_x/E_m) maxima at
339 350 nm/455 nm and similar to peak C derived from terrestrial humic sources (Coble
340 and Paula, 2007). Peak C has often been observed in various coastal (Coble, 1996) and
341 oceanic environments (Yamashita et al., 2017). C3 appeared as a fluorophore with
342 E_x/E_m wavelengths of 320 nm/390 nm and was similar to marine humic-like
343 components from coastal environments (Yamashita and Jaffé, 2008).

344 *3.3 Variation and enrichment of CO, CDOM, DOC, and FDOM in the SML*

345 [CO] showed relatively higher mean value in the SML, where its EFs ranged from
346 0.34 to 3.6 and it had a mean EFs value of 1.3 ± 0.7 (Fig. 3). The absorption of CDOM
347 and the fluorescence intensity of FDOM components in the SML were positively
348 correlated with their respective SSW values (Fig. S2), indicating that transport of DOM
349 from the SSW to the SML is an important pathway. Up to 92% of CDOM samples were
350 enriched in the SML, with the average EF value of $a_{CDOM(254)}$ of 2.2 ± 1.2 , ranging
351 between 0.4 and 6.7. The EFs of C3, C1 and C2 were 1.6 ± 0.7 , 1.4 ± 0.6 , and 1.3 ± 0.5 ,
352 respectively. The EFs of CO, CDOM, and DOC in the SML were generally higher in

353 the ECS than those in the YS (Fig. 2 and Fig. S3). Furthermore, relatively higher
354 CDOM absorption slope mean values ($S_{275-295}$ and S_R) were observed in the SML (SSW:
355 $S_{275-295}$: 0.0206 ± 0.0068 and S_R : 1.48 ± 0.49 ; SML: $S_{275-295}$: 0.0210 ± 0.0055 and S_R :
356 1.53 ± 0.22), indicating that CDOM in the SML experienced more significant
357 photodegradation than that in the SSW. The EF of CO in the daytime (1.5 ± 0.8 , 7: 00-
358 19: 00) was 1.6 times higher than that in the nighttime (0.9 ± 0.3 , 19: 00-7: 00) (Fig.
359 3b)). The EF of CDOM in the daytime (2.3 ± 11.4) was 1.1 times higher than that in
360 the nighttime (2.1 ± 0.9) (Fig. 3b)). In addition, $[CO]_{SSW}$ in the daytime (1.39 ± 0.47
361 nmol L^{-1}) was 1.3 times higher than that in the nighttime ($1.05 \pm 0.22 \text{ nmol L}^{-1}$) and
362 $[CO]_{SML}$ in the daytime ($1.88 \pm 0.77 \text{ nmol L}^{-1}$) was 2.0 times higher than that in the
363 nighttime ($0.95 \pm 0.29 \text{ nmol L}^{-1}$).

364 *3.4 Variation of sea-to-air flux of CO*

365 The atmospheric mixing ratios ($[CO]_{\text{atm}}$) of the eastern marginal seas of China
366 ranged from 239 to 900 ppbv, with an average of 602 ± 164 ppbv ($n = 69$; Fig. 2) during
367 winter. $[CO]_{\text{atm}}$ measured at station A1 in the YS (the highest concentration) was nearly
368 4 times higher than that measured at station T2 in the ECS (the lowest concentration).
369 YS showed higher CO mixing ratios (mean value: 423 ppbv in 2007; 657 ppbv in 2019)
370 than ECS (mean value: 252 ppbv in 2007; 476 ppbv in 2019) in this study and a previous
371 study (Yang et al., 2010), indicating that $[CO]_{\text{atm}}$ was relatively higher in the YS than
372 the ECS. Generally, $[CO]_{\text{atm}}$ showed a significant decreasing trend from the northern to
373 the southern regions in the eastern marginal seas of China (Fig. 2).

374 The instantaneous sea-to-air fluxes of CO ranged from -1.75 to $39.78 \text{ nmol m}^{-2} \text{ h}^{-1}$
375 1 in the SML ($4.96 \pm 7.35 \text{ nmol m}^{-2} \text{ h}^{-1}$) and from -0.04 to $34.18 \text{ nmol m}^{-2} \text{ h}^{-1}$ in the
376 SSW ($7.40 \pm 7.31 \text{ nmol m}^{-2} \text{ h}^{-1}$). Higher fluxes mostly occurred in the southernmost
377 part of the survey area in the ECS (Fig. 2). Although the concentrations of $[\text{CO}]_{\text{atm}}$ in
378 the northern region (YS) were generally higher than those in the southern region (ECS),
379 the sea-to-air fluxes of CO in the SML in the southern region ($6.94 \pm 9.61 \text{ nmol m}^{-2} \text{ h}^{-1}$
380 1) were 3.5 times higher than that in the northern region ($1.97 \pm 2.11 \text{ nmol m}^{-2} \text{ h}^{-1}$),
381 indicated that the sea-to-air flux of CO did not followed $[\text{CO}]_{\text{atm}}$ shown in Fig. 2.

382 *3.5 CO production and consumption*

383 The photoproduction rate of CO (K_{photo}) under solar irradiance ranged from 0.71
384 to $1.05 \text{ nmol L}^{-1} \text{ h}^{-1}$ ($0.86 \pm 0.12 \text{ nmol L}^{-1} \text{ h}^{-1}$) and 0.71 to $1.27 \text{ nmol L}^{-1} \text{ h}^{-1}$ (1.03 ± 0.16
385 $\text{nmol L}^{-1} \text{ h}^{-1}$) during the in-situ incubation experiments in the SSW and the SML,
386 respectively, as shown in Fig. 4a) and Table S4. The mean value of K_{photo} in the SML
387 was slightly higher than that in the SSW, but the τ_{prod} was lower in the SML (1.35 h)
388 than in the SSW (1.22 h). In addition, a significant relationship was observed between
389 the light-normalized CO production rates between the SML and the SSW ($r = 0.408$, p
390 < 0.01 , $n = 6$) during winter. The dark production rates of CO (k_{dark}) ranged from -0.01
391 to $4.81 \text{ nmol L}^{-1} \text{ d}^{-1}$, with a mean value of $1.25 \pm 2.34 \text{ nmol L}^{-1} \text{ d}^{-1}$ in the SSW (Table
392 S3). However, no significant dark production was observed in the SML water samples,
393 which indicated that dark production may be the main factor controlling CO
394 concentrations in deeper seawater.

395 The microbial consumption rates of CO in the SML varied greatly (0.18 ± 0.05
396 $\text{nmol L}^{-1} \text{h}^{-1}$), higher than the average in the SSW ($0.13 \pm 0.03 \text{ nmol L}^{-1} \text{h}^{-1}$) (Fig. 4b).
397 CO photoproduction rates were 5.7 times higher than CO consumption rates in the SML,
398 and CO photoproduction rates were 6.6 times higher than CO consumption rates in the
399 SSW. The turnover times driven by microorganism (τ_{bio}), i.e., the reciprocal of k_{bio} ,
400 were $8.9 \pm 2.9 \text{ h}$ and $11.9 \pm 5.4 \text{ h}$ in the SML and the SSW, respectively. τ_{bio} in the SML
401 and the SSW ranged between 1.43 and 3.78 d^{-1} ($2.76 \pm 0.80 \text{ d}^{-1}$) and between 1.17 and
402 3.48 d^{-1} ($2.46 \pm 0.88 \text{ d}^{-1}$), respectively, higher than those observed in the Arctic marginal
403 sea ($0.96 \pm 0.29 \text{ d}^{-1}$; Xie et al., 2005), but lower than those in the Northwest Atlantic
404 Ocean ($6.24 \pm 5.76 \text{ d}^{-1}$; Xie et al., 2005) and the China shelf sea ($4.80 \pm 1.82 \text{ d}^{-1}$; Zhang
405 et al., 2019). The maximum k_{bio} value appeared at the near-shore station B1 and the
406 minimum value at the offshore station S6 in the SML (Table S3). Thus, the bacterial
407 consumption rate constant of CO was low in oligotrophic open ocean regions but higher
408 in productive coastal areas. Since the CO photoproduction rate in the SSW at the near-
409 shore station B1 was lower than that of the near-shore station E2 and its CO
410 consumption ability was much stronger, the seawater concentration of CO at coastal
411 station E2 (1.62 nmol L^{-1}) was higher than that at coastal station B1 (1.51 nmol L^{-1}).

412 *3.6 Primary factors controlling the distribution of the optical parameters of DOM and* 413 *CO and their EFs*

414 Negative relationships were observed between salinity and $a_{\text{CDOM}}(254)$ (SSW: $p <$
415 0.01 , $r = -0.715$, $n = 62$; SML: $p = -0.045$, $n = 52$), $a_{\text{CDOM}}(355)$ (SSW: $p < 0.01$, $r =$

416 -0.622 ; SML: $r = -0.146$), and the C1 (SSW: $p < 0.01$, $r = -0.758$; SML: $r = -0.158$),
417 C2 (SSW: $p < 0.01$, $r = -0.341$; SML: $r = -0.106$), and C3 (SSW: $p < 0.01$, $r = -0.851$;
418 SML: $r = -0.154$) components in SSW and SML (Table 1). High and low fluorescence
419 levels of these three components were usually found at sites with low and high salinities,
420 respectively (Fig. 2). These results indicated that riverine inputs mainly determined the
421 distributions of CDOM and FDOM. $a_{\text{CDOM}(254)}$ and all three fluorescence components
422 were also positively correlated with SUVA_{254} (Table 1), indicating that CDOM showed
423 higher aromaticity and humification in the eastern marginal seas of China. In addition,
424 we observed a significant positive relationship between $a_{\text{CDOM}(254)}$ and Chl-*a* in the
425 SSW ($p < 0.01$, $r = 0.333$, $n = 62$), suggesting that phytoplankton biomass and biological
426 processes played an essential role in generating new CDOM and controlling the
427 distribution of CDOM in winter.

428 Although significant CO production via CDOM photodegradation has been
429 recorded in estuarine systems (Stubbins et al., 2011), no significant relationships were
430 observed between [CO] and $a_{\text{CDOM}(254)}$ in either the SSW or the SML in our study
431 regions. $a_{\text{CDOM}(254)}$ ($p < 0.01$, $r = -0.419$) and the marine humic-like C3 ($p < 0.01$, $r =$
432 -0.201) were both negatively correlated with the flux of CO in the SML (Fig. 5a and
433 b). The flux of CO was positively related to temperature ($p < 0.01$, $r = 0.511$) and
434 salinity ($p < 0.01$, $r = 0.338$) in the SSW (Fig. 5), but the EF of CO showed no significant
435 relationship with surface water temperature, salinity, or mean wind speed during
436 sampling (Fig. 5d and 5f).

437 **4. Discussion**

438 *4.1 CO and DOM distribution and enrichment in the SML*

439 [CO] showed great seasonal and diel variability, as well as variability between
440 ocean regions. [CO]_{SSW} mean value in the YS in January 2020 (1.23 ± 0.40 nmol L⁻¹)
441 was higher than in September 2010 (1.05 nmol L⁻¹, Zhao et al., 2015). [CO]_{SSW} mean
442 value in the ECS during winter (1.23 ± 0.45 nmol L⁻¹) was also higher than in October
443 2021 (0.97 ± 0.86 nmol L⁻¹, Yang et al., 2024). Globally, [CO]_{SSW} mean value (1.23
444 nmol L⁻¹) in the eastern marginal seas of China was similar to that observed in the Bohai
445 Sea and the YS during autumn (Zhang et al., 2019, 1.22 nmol L⁻¹) and the Arctic waters
446 of the Amundsen Gulf (Beaufort Sea) in September/October (Xie et al., 2009, 0.17–
447 1.34 nmol L⁻¹), but was relatively lower than the Eastern Indian Ocean (Xu et al., 2023,
448 1.92 nmol L⁻¹). The Eastern Indian Ocean, on the other hand, had a salinity of
449 approximately 34 and a relatively high temperature (around 29°C) in autumn 2020 (Xu
450 et al., 2023). Tropical and subtropical open ocean regions were generally less affected
451 by terrestrial influences compared to estuarine, coastal and high-latitude areas. CO
452 production and fluxes normalized to discharge are usually higher in warmer waters
453 (Kieber et al., 2014), presumably also partly due to temperature controls on dissolution
454 (Johnson et al., 1996). Therefore, the relatively higher concentration of [CO]_{SSW} in the
455 open ocean (ECS) might be characterized by the relatively high seawater temperature
456 and/or strong production processes during our sampling period.

457 Our results showed that there was no significant enrichment of CO in SML during
458 the investigation, and CO enrichment in SML only occurred at 25 stations. Earlier
459 studies have shown that the diurnal variation of $[CO]_{SSW}$ in sea surface concentration,
460 which was first noted in the Atlantic Ocean by Swinnerton et al. (1970), with a
461 characteristic minimum just before dawn and a maximum in the early afternoon. This
462 cycle was subsequently observed in other expeditions in both the Pacific and Atlantic
463 Oceans (Matsueda et al., 2000; Rhee, 2000; Ren et al., 2010; Yang et al., 2010; Yang
464 et al., 2011). Here, $[CO]_{SSW}$, $[CO]_{SML}$ and the EFs of CO also showed strong diurnal
465 fluctuations (Fig. 3, Section 3.1 and 3.3). Significant positive relationships were
466 observed between the EFs of CO and the net solar irradiance (Table 3), likely resulting
467 from the sunlight-induced photochemical production of CO during daytime and the
468 stronger microbial consumption at night. The higher EF values of CO also occurred in
469 the daytime (Fig. 3b), suggesting that sufficient light and higher temperatures combined
470 to facilitate the photoproduction of CO and its enrichment in the SML.

471 CO, CDOM, and FDOM were more frequently enriched in the ECS (Fig. 2). DOC
472 and CDOM decreased from coastal regions to the open ocean, and decreased from the
473 northern sampling area (the YS) to the southern sampling area (the ECS) in both the
474 SSW and the SML (Fig. 2), which was likely due to the input from the land-based
475 sources (Yang et al., 2022). Moreover, atmospheric deposition of organic carbon and
476 nutrients was found to peak in winter over the coastal ECS (Wang et al., 2019).
477 Although the source of CDOM originated from allochthonous terrestrial sources in the
478 ECS and the YS (Yang et al., 2021), the sink of CDOM in the ECS was more dominated

479 by photochemical degradation processes (Zhu et al., 2018). The EF of marine humic-
480 like Component 3 was significantly higher than the other fluorescence components (1.6
481 vs. 1.4 and 1.3), indicating that in-situ autochthonous DOM was more strongly enriched
482 in the SML than terrestrial DOM. Thus, CO, CDOM, and FDOM were more frequently
483 enriched in the open ocean (ECS), which was attributed mainly to the significant local
484 photoproduction. Further, one note of the study of gases in the SML is that gases
485 supersaturated with respect to their atmospheric concentrations, including CO, are
486 inevitably lost from SML samples during sampling, depending on environmental
487 conditions such as water temperature and wind. For example, in case of dimethylsulfide
488 (DMS), a volatile gas with large concentration difference between the atmosphere and
489 the ocean, Yang et al. (2001) and Yang and Tsunogai (2005) showed about 50–70%
490 and 60% (mean) of loss from SML samples collected using a mesh screen at 0–15°C
491 and at a water temperature of 10°C and wind speed of 4 m s⁻¹, respectively. A mesh
492 screen was also used in this study, and parameters such as [CO]_{SML} and the EF of CO
493 may have been underestimated.

494 *4.2 Photochemical and dark CO production and biological CO consumption in the SML* 495 *and the SSW*

496 Photochemical CO production is the most active in the SML, the mean
497 photoproduction rate of CO in the SML was 1.1 times higher than that in the SSW in
498 the eastern marginal seas of China. CO in our study region showed a longer turnover
499 time than the findings of Sugai et al. (2021) in Sagami Bay, Japan ($\tau_{\text{prod}} = 0.09$ h), which

500 is probably due to the relatively low photochemical CO production rate in the SML
501 and/or the higher photochemical degradability of CDOM in the SML under more
502 intense light conditions in our study region.

503 The turnover times driven by sea-to-air exchange were much longer than those of
504 microbial consumption, about 219 h and 1029 h in the SSW and SML, respectively.
505 This indicated that microbial removal of CO was much faster than sea-to-air exchange,
506 which may make the latter a subordinate pathway for CO removal in our study regions.
507 Relatively higher microbial consumption rate of CO in marine systems has been
508 historically attributed to higher Chl-*a*, but lower salinity level (Xie et al., 2009; Yang
509 et al., 2010; Xu et al., 2023). In addition, the heterotrophic bacterial abundance in the
510 SML was ~ 7.5 times greater than in the SSW and the ECS in March 2017 (Sun et al.,
511 2020). The SML is an aggregate-enriched biofilm environment with distinct microbial
512 communities, the diversity of which can differ significantly from underlying waters
513 (Liss and Duce, 2005; Cunliffe et al., 2013). This higher abundance of bacteria could
514 result in the rapid consumption of CO, along with a wide variety of other organic
515 substances in the SML. Moreover, elevated nutrient concentrations can stimulate the
516 growth of phytoplankton, biological activity, and subsequently lead to abundant
517 primary production in the SML (Yang et al., 2022). Therefore, compared to the SSW,
518 the elevated DOM concentrations and bacteria abundances could enhance the
519 influences of photoproduction and microbial consumption on CO cycling processes in
520 the SML.

521 *4.3 Implications of CO sea-to-air exchange and emission to the atmosphere*

522 Based on the areas of the ECS ($7.7 \times 10^5 \text{ km}^2$) and YS ($3.8 \times 10^5 \text{ km}^2$) and their
523 respective CO sea-to-air fluxes, the releases of CO from the ECS and YS to the
524 atmosphere were estimated to range from 3 to 230 Mg CO-C month⁻¹ (Mg = 10^6 g) and
525 from -0.2 to 880 Mg CO-C month⁻¹, with averages of 70 Mg CO-C month⁻¹ and 10 Mg
526 CO-C month⁻¹, respectively. Clearly, the average annual release of CO to the
527 atmosphere in the ECS was much higher (nearly 7 times) than in the YS. Yang et al.
528 (2010) suggested that [CO]_{SSW} was the main factor affecting the sea-to-air flux of CO,
529 but [CO]_{SSW} in the ECS was similar to that in the YS. The lower temperatures and
530 especially reduced wind speeds may hinder its outgassing to the atmosphere. The higher
531 [CO]_{atm} at the northern stations (the YS) was representative of the regionally polluted
532 continental outflow air mass due to the anthropogenic activity in East Asia. Therefore,
533 [CO]_{atm} values in the YS were heavily dependent on land anthropogenic input, but in
534 the ECS, the distribution of [CO]_{atm} was more dependent on the sea-to-air flux of CO.

535 As noted above, the most probable sources of CO in the SML of these sea regions
536 are in-situ photoproduction from DOM and/or vertical export through underlying SSW
537 water. Actually, surface-active surfactants are ubiquitous and accumulate in the
538 uppermost < 1000 μm in seawater (Rickard et al., 2019), where they slow the rate of
539 gas exchange between seawater and air (Cunliffe et al., 2013). Although surfactants
540 represent only a fraction of the dissolved organic matter pool, Rickard et al. (2022)
541 observed that the first-order estimates of the potential suppression of the gas transfer
542 velocity (kw) by photo-derived surfactants were 12.9%–22.2% in coastal North Sea

543 water. The highest SML enrichments in surfactants have been seen in low productivity,
544 oligotrophic regions away from terrestrial influences, where surfactant concentrations
545 in SSW are generally low (Wurl et al., 2016). Pereira et al. (2018) also noted that the
546 observed reduction in the air-to-sea CO₂ exchange in the Atlantic Ocean was due to
547 biological surfactants acting as physical barriers and altering turbulent transfer near the
548 water surface. Therefore, the relatively lower fluxes of CO observed in the YS may
549 indicate that seawater contains lots of DOM (surfactants) in the SML. Despite the clear
550 importance of surfactants at the sea-to-air interface, we did not conduct surfactant-
551 specific analyses due to the analytical limitations. In our experiments, the CO flux
552 varied by 131% in winter. The negative correlations between a_{CDOM}(254) and the sea-
553 to-air flux of CO, and between marine humic-like C3 and the sea-to-air flux of CO
554 suggested that CDOM concentration may reduce the CO sea-to-air gas exchange rate
555 in our study regions (Fig. 5a and 5b). In addition, low wind speeds may lead to high
556 DOM enrichment, but in the meantime give rise to low sea-to-air fluxes as well.
557 Therefore, due to the complexity of the DOM pool in the SML and its may result in
558 decreased sea-to-air flux of CO, more measurements are needed to validate our
559 conceptual model and provide a better understanding of the flux measurements of CO
560 in the SML.

561 During our study period (winter), surface seawater temperature showed substantial
562 spatial fluctuations (from 2.08°C in the YS to 23.80°C in the ECS) due to the broad
563 investigation range. In our previous manuscript (Yang et al., 2022), we observed that
564 the relatively higher enrichment of nutrients in summer which could enhance

565 phytoplankton growth and promote DOM production in the SML; and stronger
566 enrichment and photochemical processes occur in the SML, resulting in the relatively
567 accelerated enrichment of more marine local production DOM in the SML than the
568 SSW. During warm seasons, stronger light and temperature may change the relative
569 importance of light production, microbial production and DOM (surfactants)
570 composition and inhibition of CO flux. Therefore, DOM inhibits CO flux still requires
571 further verification in other seasons and regions.

572 *4.4 Modeling of CO dynamics in the SML and the SSW*

573 All sources and sinks, including photoproduction and dark production, microbial
574 consumption and sea-to-air emission, should be considered in estimating CO dynamics
575 in the SML and SSW (Fig. 6). The effective solar illumination period of each day was
576 approximately 12 h, and based on this the average photoproduction rates in the SML
577 and the SSW were calculated to be $12.41 \pm 1.87 \text{ nmol L}^{-1} \text{ d}^{-1}$, $10.32 \pm 1.48 \text{ nmol L}^{-1} \text{ d}^{-1}$,
578 respectively. In the SSW, the ratio of photoproduction to dark production (1.88 ± 2.89
579 $\text{nmol L}^{-1} \text{ d}^{-1}$) was about 4:1, and dark production accounted for about 15% of the total
580 production. No dark production of CO was observed in the SML. CO photoproduction
581 was lower in deeper water, while dark production was higher. The calculated
582 contribution of dark production to CO production in this study was similar to that for
583 the St. Lawrence estuary (14%; Zhang and Xie, 2012) but much lower than for the
584 Eastern Indian Ocean (20%; Xu et al., 2023). These were because dark production
585 needs to be given more weight in estimating its contribution to the total production of

586 CO in the deeper waters of the ocean than in estuaries (Xu et al., 2023). The total
587 removal rates of CO were about $2.64 \text{ nmol L}^{-1} \text{ d}^{-1}$ and $2.88 \text{ nmol L}^{-1} \text{ d}^{-1}$ in the SSW and
588 the SML, respectively, including the microbial consumption rates of $2.46 \pm 0.88 \text{ nmol}$
589 $\text{L}^{-1} \text{ d}^{-1}$ and $2.76 \pm 0.80 \text{ nmol L}^{-1} \text{ d}^{-1}$ in the SSW and the SML, respectively. The sea-to-
590 air exchange rates were $0.18 \pm 0.18 \text{ nmol L}^{-1} \text{ d}^{-1}$ in the SSW and $0.12 \pm 0.18 \text{ nmol L}^{-1}$
591 d^{-1} in the SML. The turnover of CO occurred faster in the SML environment than in the
592 SSW (~ 1.2 times). Microbial consumption was the primary sink of CO, accounting for
593 about 95% of CO removal, indicating that the biogeochemical cycling of CO is almost
594 entirely contained within seawater and only a small amount of CO is released into the
595 atmosphere (Xie et al., 2005; Yang et al., 2010; Zhang et al., 2019; Xu et al., 2023).
596 The production rates of CO in both SML and SSW significantly exceed the loss rates,
597 this could lead to the accumulation of CO in these systems. Therefore, CO balance in
598 the ECS and YS indicated that the underlying loss of CO (via sea-to-air flux and
599 biodegradation) was slower than the production of CO in the SML, therefore, a positive
600 CO balance was maintained in the SML.

601 The average annual photoproduction, microbial consumption, and sea-to-air flux
602 of CO in the SSW were about 3.02, 1.58, and 0.04 Gg CO-C month⁻¹, respectively,
603 based on the area of the survey region ($\sim 1.2 \times 10^6 \text{ km}^2$, SSW $\sim 10 \text{ m}$). Conte et al.
604 (2019) used the NEMO-PISCES model combined with original ocean CO data
605 collected worldwide over the last 50 years, ultimately estimating that global emissions
606 of CO to the atmosphere were 4.0 Tg CO-C yr⁻¹ (Tg = 10¹² g). Based on our data, we
607 estimated the contribution of China's eastern marginal seas to global marine CO

608 emissions via sea-to-air flux to be $\sim 0.3\%$, and the YS and the ECS occupy 2.7% of
609 the global ocean area. The simulated surface CO concentrations and sea-to-air fluxes
610 based on our measured values were much smaller than those simulated by Erickson
611 (1989). In our study, CO produced can be rapidly consumed by microorganisms and
612 only a small fraction was released into the atmosphere, which may explain why the
613 relative contribution of the eastern marginal seas of China to atmospheric CO was much
614 lower than the global level.

615 Notably, the enrichment of CO in the SML was more common during the daytime
616 when photochemical processes were more active, but natural sunlight can inhibit the
617 microbial consumption of CO. CO was maximal in the SML, leading to the significant
618 enrichment and supersaturation. CDOM in the SML experienced more significant
619 photodegradation than that in the SSW, as can be seen in Section 3.3. Moreover,
620 researchers assumed that biological, chemical and physical processes in the SML are
621 controlled by changes in DOM concentration at this uppermost thin boundary layer
622 between the ocean and the atmosphere (Cunliffe et al., 2013). We found that
623 autochthonous humic-like DOM was more enriched in the SML than terrestrial DOM,
624 indicating that it could be an indispensable part of CO photoproduction (Yang et al.,
625 2022). Solar irradiance was positively related to the EFs of CO (Table 3), suggesting
626 that the integrated solar irradiance influenced CO enrichment in the SML. Moreover,
627 we did discover the potential for CDOM accumulation in the SML to prevent CO
628 emissions into the atmosphere (Section 4.3). Therefore, CDOM accumulation and the

629 production rates of CO in the SML significantly exceed the loss rates, which could lead
630 to the significant accumulation of CO in the SML, especially in the daytime.

631 **5. Conclusions**

632 This study is the first comprehensive analysis of CO distribution, loss, and
633 production in both the SML and SSW, as well as sea-to-air CO flux in the ECS and YS
634 during winter. $[CO]_{SSW}$, $[CO]_{SML}$, CDOM, FDOM, and DOC generally decreased from
635 coastal regions toward the open ocean. However, the EFs of CO, CDOM, FDOM, and
636 DOC were significantly higher in offshore areas, indicating that stronger enrichment
637 and/or production processes in the SML are more common in open waters than
638 nearshore. CDOM absorption slope mean values ($S_{275-295}$ and S_R) showed that CDOM
639 in the SML experienced more extensive photodegradation than in the SSW. Notably,
640 the EF of the marine humic-like component C3 was significantly higher than other
641 fluorescence components, suggesting that in-situ autochthonous DOM was more
642 strongly enriched in the SML compared to terrestrial DOM. Significant negative
643 correlations were observed between $a_{CDOM}(254)$ and sea-to-air CO flux, as well as
644 between sea-to-air CO flux and humic-like C3 in the SML, indicating that the open sea
645 had lower CDOM concentrations but greater suppression of CO gas transfer compared
646 to nearshore waters. This suggests that DOM enrichment may influence CO emissions
647 to the atmosphere in the SML. The diurnal variability in CO EF and $[CO]_{SML}$ indicates
648 that in-situ photoproduction processes are vital in shaping CO distribution within the
649 SML. Our results demonstrate a complex interaction between DOM enrichment and

650 sea-to-air CO fluxes in the SML, which should be incorporated into future carbon
651 budget models for more accurate assessments of carbon cycling in marine environments.

652 **Author contribution**

653 Lin Yang: Conceptualization, Writing-Original Draft, Writing-Review and Editing

654 Bin Yang: Writing-Review and Editing

655 Jing Zhang: Writing-Review and Editing, Funding acquisition

656 Anja Engel: Writing-Review and Editing

657 Gui-Peng Yang: Writing-Review and Editing, Supervision

658

659 **Competing interests**

660 The authors declare that they have no known competing financial interests or personal
661 relationships that could have appeared to influence the work reported in this paper.

662 **Acknowledgment**

663 We are grateful to the captain and crew of the R/V “*Dong Fang Hong 3*” for their
664 help and cooperation during the in-situ investigation. This study was financially
665 supported by the National Natural Science Foundation of China (Grant No. 42330402),
666 the National Key Research and Development Program (Grant No. 2016YFA0601300),
667 and the Natural Science Research Project of Jiangsu Province Higher Education
668 Institutions (25KJD170004).

669

References

- 670 Chen, C.T.A., 2009. Chemical and physical fronts in the Bohai, Yellow and East China
671 seas. *J. Mar. Syst.* 78(3), 394–410. doi: 10.1016/j.jmarsys.2008.11.016
- 672 Chen, Y., Yang, G., Xia, Q., Wu, G., 2016. Enrichment and characterization of
673 dissolved organic matter in the surface microlayer and subsurface water of the
674 South Yellow Sea. *Mar. Chem.* 182(Mar. 20), 1–13. doi:
675 10.1016/j.marchem.2016.04.001
- 676 Chowdhury, S., 2013. Trihalomethanes in drinking water: effect of natural organic
677 matter distribution. *WATER SA*, 39, 1–7. doi: 10.4314/wsa.v39i1.1
- 678 Coble, P.G., 1996. Characterization of marine and terrestrial DOM in seawater using
679 excitation-emission matrix spectroscopy. 51(4), 325–346. doi: 10.1016/0304-
680 4203(95)00062-3
- 681 Coble, P.G., Paula, G., 2007. Marine optical biogeochemistry: the chemistry of ocean
682 color. *Cheminform* 38(2), 402–418. doi: 10.1002/chin.200720265
- 683 Conte, L., Szopa, S., Séférian, R., Bopp, L., 2019. The oceanic cycle of carbon
684 monoxide and its emissions to the atmosphere. *Biogeosciences*, 16(4), 881–902.
685 doi: 10.5194/bg-16-881-2019
- 686 Cordero, P.R.F., Bayly, K., Leung, P.M., Huang, C., Greening, C., 2019. Atmospheric
687 carbon monoxide oxidation is a widespread mechanism supporting microbial
688 survival. *ISME J.* 13(14). doi: 10.1038/s41396-019-0479-8
- 689 Cory, R.M., Kling, G.W., 2018. Interactions between sunlight and microorganisms
690 influence dissolved organic matter degradation along the aquatic continuum.
691 *Limnol. Oceanogr. Lett.* 3(3), 102–116. doi: 10.1002/lol2.10060

692 Cunliffe, M., Engel, A., Frka, S., Gašparovi, B., Guitart, C., Murrell, J.C., Salter, M.,
693 Stolle, C., Upstill-Goddard, R., Wurl, O., 2013. Sea surface microlayers: A unified
694 physicochemical and biological perspective of the air-ocean interface. *Prog.*
695 *Oceanogr.* 109, 104–116. doi: 10.1016/j.pocean.2012.08.004

696 Cunliffe, M., Upstill-Goddard, R.C., Murrell, J.C., 2011. Microbiology of aquatic
697 surface microlayers. *FEMS Microbiol. Rev.* 35(2), 233–246. doi:
698 10.1111/j.1574 - 6976.2010.00246.x

699 Cunliffe, M., Wurl, O., 2014. Guide to best practices to study the ocean’s surface.
700 Occasional Publications of the Marine Biological Association of the United
701 Kingdom, Plymouth, UK. 118 pp.

702 Doney, S.C., Najjar, R.G., Stewart, S., 1995. Photochemistry, mixing and diurnal cycles
703 in the upper ocean. *J. Mar. Res.* 53(3), 341–369. doi: 10.1357/0022240953213133

704 Edson, J.B., Fairall, C.W., Bariteau, L., Zappa, C.J., Cifuentes-Lorenzen, A., McGillis,
705 W.R., Pezoa, S., Hare, J.E., Helmig, D., 2011. Direct covariance measurement of
706 CO₂ gas transfer velocity during the 2008 Southern Ocean Gas Exchange
707 Experiment: Wind speed dependency. *J. Geophys. Res.* 116(C4), 1943–1943. doi:
708 10.1029/2011jc007022

709 Engel, A., Galgani, L., 2016. The organic sea-surface microlayer in the upwelling
710 region off the coast of Peru and potential implications for air–sea exchange
711 processes. *Biogeosciences* 13, 989–1007. doi: 10.5194/bg-13-989-2016

712 Engel, A., Bange, H.W., Cunliffe, M., Burrows, S.M., Friedrichs, G., Galgani, L.,
713 Herrmann, H., Hertkorn, N., Johnson, M., Liss, P.S., Quinn, P.K., Schartau, M.,
714 Soloviev, A., Stolle, C., Upstill-Goddard, R. C., van Pinxteren, M., Zäncker, B.

715 2017. The Ocean's Vital Skin: Toward an Integrated Understanding of the Sea
716 Surface Microlayer, *Front. Mar. Sci.*, 4. doi: 10.3389/fmars.2017.00165

717 Erickson, D.J., 1989. Ocean to atmosphere carbon monoxide flux: Global inventory
718 and climate implications. *Global Biogeochem. Cyc.* 3(4), 305–314. doi:
719 10.1029/GB003i004p00305

720 Fichot, C.G., Miller, W.L., 2010. An approach to quantify depth-resolved marine
721 photochemical fluxes using remote sensing: application to carbon monoxide (CO)
722 photoproduction. *Remote Sens. Environ.* 114, 1363–1377. doi:
723 10.1016/j.rse.2010.01.019

724 Garrett, W.D., 1965. Collection of slick-forming materials from the sea surface. *Limnol.*
725 *Oceanogr.* 10(1965), 602–605. doi: 10.2307/2833459

726 Gros, V., Peeken, I., Bluhm, K., Zöllner, E., Sarda-Esteve, R., Bonsang, B., 2009.
727 Carbon monoxide emissions by phytoplankton: evidence from laboratory
728 experiments. *Environ. Chem.* 6, 369–379. doi: 10.1071/EN09020

729 Guallar, C., Flos, J., 2019. Linking phytoplankton primary production and
730 chromophoric dissolved organic matter in the sea. *Prog. Oceanogr.* 176, 102116.
731 doi: 10.1016/j.pocean.2019.05.008

732 Huang, Y.J., Brimblecombe, P., Lee, C.L., Latif, M.T., 2015. Surfactants in the sea-
733 surface microlayer and sub-surface water at estuarine locations: Their
734 concentration, distribution, enrichment, and relation to physicochemical
735 characteristics. *Mar. Pollut. Bull.* 97(1–2), 78–84. doi:
736 10.1016/j.marpolbul.2015.06.031

737 Jones, R.D., Amador, J.A., 1993. Methane and carbon monoxide production, oxidation,
738 and turnover times in the Caribbean Sea as influenced by the Orinoco River. *J.*
739 *Geophys. Res.* 98(C2), 2353–2359. doi: 10.1029/92JC02769

740 Johnson, J.E., Bates, T.S., 1996. Sources and sinks of carbon monoxide in the mixed
741 layer of the tropical South Pacific Ocean. *Global Biogeochem. Cy.* 10(2), 347–
742 359. doi: 10.1029/96GB00366

743 Kettle, A.J., 2005. Diurnal cycling of carbon monoxide (CO) in the upper ocean near
744 Bermuda. *Ocean Model.* 8(4), 337–367. doi: 10.1016/j.ocemod.2004.01.003

745 Kieber, D.J., Miller, G.W., Neale, P.J., Mopper, K., 2014. Wavelength and temperature-
746 dependent apparent quantum yields for photochemical formation of hydrogen
747 peroxide in seawater. *Env. Sci.: Processes Impacts.* doi: 10.1039/C4EM00036F

748 Li, Y., He, Z., Yang, G.P., Wang, H., Zhuang, G.C., 2019. Volatile halocarbons in the
749 marine atmosphere and surface seawater: diurnal and spatial variations and
750 influences of environmental factors. *Atmos. Environ.* 214, 116820.
751 10.1016/j.atmosenv.2019.116820

752 Li, Y., Fichot, C.G., Geng, L., Scarratt, M.G., Xie, H., 2020. The Contribution of
753 Methane Photoproduction to the Oceanic Methane Paradox. *Geophys. Res. Lett.*
754 47(14), 1–10. doi: 10.1029/2020GL088362

755 Liss, P.S., Merlivat, L., 1986. Air-sea gas exchange rates: Introduction and synthesis.
756 In P. Buat-Ménard (Ed.), *The role of air-sea exchange in geochemical cycling*, (pp.
757 113–127). Dordrecht, Netherlands: Springer. Retrieved from
758 papers3://publication/uuid/BAFDE7E6-A29C-466C-B1CD-2A7DAFF930D5

759 Liss, P.S., Duce, R.A., (Eds) 1997. The sea surface and global change. Cambridge, UK:
760 Cambridge University Press.

761 Liss, P.S., Duce, R.A., 2005. The Sea Surface and Global Change, Cambridge
762 University Press, UK, ISBN-13: 978-0511525025

763 Lønborg, C., Álvarez-Salgado, X.A., Duggan, S., Carreira, C., 2018. Organic matter
764 bioavailability in tropical coastal waters: The Great Barrier Reef. *Limnol.*
765 *Oceanogr.* 63, 1015–1035. doi: 10.1002/lno.10717

766 Ma, Q.Y., Yang, G.P., 2023. Roles of phytoplankton, microzooplankton, and bacteria
767 in DMSP and DMS transformation processes in the East China Continental Sea.
768 *Prog. Oceanogr.* 103003. doi: 10.1016/j.pocean.2023.103003

769 Mopper, K., Kieber, D.J., 2002. Photochemistry and cycling of carbon, sulfur, nitrogen
770 and phosphorus. In: Hansell, D.A., Carlson, C.A. (Eds.), *Biogeochemistry of*
771 *Marine Dissolved Organic Matter*. AP. doi: 10.1016/b978-012323841-2/50011-7

772 Nelson, E.D., McConnell, L.L., Baker, J.E., 1998. Diffusive Exchange of Gaseous
773 Polycyclic Aromatic Hydrocarbons and Polychlorinated Biphenyls Across the
774 Air–Water Interface of the Chesapeake Bay. *Environ. Sci. Technol.* 32(7), 912–
775 919. doi: 10.1021/es9706155

776 Nguyen, N.H., Turner, A.J., Yin, Y., Prather, M.J., Frankenberg, C., 2020. Effects of
777 chemical feedbacks on decadal methane emissions estimates. *Geophys. Res. Lett.*
778 47(3), e2019GL085706. doi: 10.1029/2019GL085706

779 Obernosterer, I., Catala, P., Reinthaler, T., Herndl, G.J., Lebaron, P., 2006. Enhanced
780 heterotrophic activity in the surface microlayer of the Mediterranean Sea. *Aquat.*
781 *Microb. Ecol.* 39, 293–302. doi: 10.3354/ame039293

782 Obernosterer, I., Catala, P., Lami, R., Caparros, J., Ras, J., Bricaud, A., Dupuy, C., van
783 Wambeke, F., Lebaron, P., 2008. Biochemical characteristics and bacterial
784 community structure of the sea surface microlayer in the South Pacific Ocean.
785 *Biogeosciences* 5, 693–705. doi: 10.5194/bg-5-693-2008

786 Orellana, M.V., Matrai, P.A., Leck, C., Rauschenberg, C.D., Lee, A.M., Coz, E., 2011.
787 Marine microgels as a source of cloud condensation nuclei in the high Arctic. *Proc.*
788 *Natl. Acad. Sci.* 108, 13612–13617. doi: 10.1073/pnas.1102457108

789 Pereira, R., Schneider-Zapp, K., Upstill-Goddard, R.C., 2016. Surfactant control of gas
790 transfer velocity along an offshore coastal transect: results from a laboratory gas
791 exchange tank. *Biogeosciences* 13, 3981–3989. doi: 10.5194/bg-13-3981-2016

792 Pereira, R., Ashton, I., Sabbaghzadeh, B., Shutler, J.D., Upstill-Goddard, R.C., 2018.
793 Reduced air–sea CO₂ exchange in the Atlantic Ocean due to biological surfactants.
794 *Nat. Geosci.* 11, 492–496. doi: 10.1038/s41561-018-0136-2

795 Ren, C., Yang, G., Lu, X., 2014. Autumn photoproduction of carbon monoxide in
796 Jiaozhou Bay China. *J. Ocean U. China*, 13(3), 428–436. doi: 10.1007/s11802-
797 014-2225-1

798 Rickard, P.C., Uher, G., Upstill-Goddard, R.C., Frka, S., Mustaffa, N.I.H., Banko-Kubis,
799 H.M., Hanne Marie, B.K., Ana Cvitesic, K., Blazenka, G., Christian, S., Oliver,
800 W., Ribas-Ribas, M., 2019. Reconsideration of seawater surfactant activity

801 analysis based on an inter-laboratory comparison study. *Mar. Chem.* 208, 103–111.
802 doi: 10.1016/j.marchem.2018.11.012

803 Rickard, P.C., Uher, G., Upstill Goddard, R.C., 2022. Photo reactivity of surfactants in
804 the sea surface microlayer and subsurface water of the Tyne estuary, UK. *Geophys.*
805 *Res. Lett.* 49(4), e2021GL095469. doi: 10.1029/2021GL095469

806 Sabbaghzadeh, B., Upstill-Goddard, R.C., Beale, R., Pereira, R., Nightingale, P.D.,
807 2017. The Atlantic Ocean surface microlayer from 50°N to 50°S is ubiquitously
808 enriched in surfactants at wind speeds up to 13 m s⁻¹. *Geophys. Res. Lett.* 44(6),
809 2852–2858. doi: 10.1002/2017GL072988

810 Shaharom, S., Latif, M.T., Khan, M.F., Yusof, S.N.M., Sulong, N.A., Wahid, N.B.A.,
811 Uning, R., Suratman, S., 2018. Surfactants in the sea surface microlayer,
812 subsurface water and fine marine aerosols in different background coastal areas.
813 *Environ. Sci. Pollut. Res. Int.* 25(27), 27074–27089. doi: 10.1007/s11356-018-
814 2745-0

815 Song, G., Richardson, J.D., Werner, J.P., Xie, H., Kieber, D.J., 2015. Carbon monoxide
816 photoproduction from particles and solutes in the Delaware estuary under
817 contrasting hydrological conditions. *Environ. Sci. Technol.* 49(24), 14048–14056.
818 doi: 10.1021/acs.est.5b02630

819 Stedmon, C.A., Markager, S., Bro, R., 2003. Tracing dissolved organic matter in
820 aquatic environments using a new approach to fluorescence spectroscopy. *Mar.*
821 *Chem.* 82(3–4), 239–254. doi: 10.1016/S0304-4203(03)00072-0

822 Stubbins, A., Uher, G., Kitidis, V., Law, C.S., Upstill-Goddard, R.C., Woodward,
823 E.M.S., 2006. The open-ocean source of atmospheric carbon monoxide. *Deep-Sea*
824 *Res. Part II*, 53, 1685–1694. doi: 10.1016/j.dsr2.2006.05.010

825 Stubbins, A., Law, C., Uher, G., Upstill-Goddard, R., 2011. Carbon monoxide apparent
826 quantum yields and photoproduction in the Tyne estuary. *Biogeosciences* 8, 703–
827 713. doi:10.5194/bg-8-703-2011

828 Sugai, Y., Tsuchiya, K., Shimode, S., Toda, T., 2021. Photochemical Production and
829 Biological Consumption of CO in the SML of Temperate Coastal Waters and Their
830 Implications for Air-Sea CO Exchange. *J. Geophys. Res.: Oceans* 125(4), 1–14.
831 doi: 10.1029/2019JC015505

832 Sun, H., Zhang, Y.H., Tan, S., Zheng, Y.F., Zhou, S., Ma, Q.Y., Yang, G.P., Todd, J.,
833 Zhang, X.H., 2020. DMSP-Producing Bacteria Are More Abundant in the Surface
834 Microlayer than Subsurface Seawater of the East China Sea. *Microb. Ecol.* 80,
835 350–365. doi: 10.1007/s00248-020-01507-8

836 Troxler, R.F., 1972. Synthesis of bile pigments in plants. Formation of carbon
837 monoxide and phycocyanobilin in wild-type and mutant strains of the alga,
838 *Cyanidium caldarium*. *Biochemistry* 11(23), 4235–4242. doi:
839 10.1021/bi00773a007

840 Tsai, W.T., Liu, K.K., 2003. An assessment of the effect of sea surface surfactant on
841 global atmosphere–ocean CO₂ flux. *J. Geophys. Res.: Oceans* 108, 3127. doi:
842 10.1029/2000jc000740

843 Walker, C.F., Harvey, M.J., Smith, M.J., Bell, T.G., Saltzman, E.S., Marriner, A.S.,
844 McGregor, J.A., Law, C.S., 2016. Assessing the potential for dimethylsulfide
845 enrichment at the sea surface and its influence on air–sea flux. *Ocean Sci.* 12,
846 1033–1048. doi: 10.5194/os-12-1033-2016

847 Wang, H., Sun, F., Liu, W., 2020. Characteristics of Streamflow in the Main stream of
848 Changjiang River and the Impact of the Three Gorges Dam. *Catena* 104498. doi:
849 10.1016/j.catena.2020.104498

850 Weishaar, J.L., Aiken, G.R., Bergamaschi, B.A., Fram, M.S., Fujii, R., Mopper, K.,
851 2003. Evaluation of specific ultraviolet absorbance as an indicator of the chemical
852 composition and reactivity of dissolved organic carbon. *Environ. Sci. Technol.* 37,
853 4702–4708. doi: 10.1021/es030360x

854 Wiesenburg, D.A, Guinasso, N.L., 1979. Equilibrium solubilities of methane, carbon
855 monoxide, and hydrogen in water and sea water. *J. Chem. Eng. Data* 24(4), 356–
856 360. doi: 10.1021/je60083a006

857 Wurl, O., Miller, L., Röttgers, R., Vagle, S., 2009. The distribution and fate of surface-
858 active substances in the sea-surface microlayer and water column. *Mar. Chem.* 115,
859 1–9. doi: 10.1016/j.marchem.2009.04.007

860 Wurl, O., Stolle, C., Thuoc, C.V., Thu, P.T., Mari, X., 2016. Biofilm-like properties of
861 the sea surface and predicted effects on air-sea CO₂ exchange. *Prog. Oceanogr.*
862 144, 15–24. doi: 10.1016/j.pocean.2016.03.002

863 Xie, H., Andrews, S.S., Martin, W.R., Miller, J., Zafiriou, O.C., 2002. Validated
864 methods for sampling and headspace analysis of carbon monoxide in seawater.
865 *Mar. Chem.* 77(2), 93–108. doi: 10.1016/S0304-4203(01)00065-2

866 Xie, H., Zafiriou, O.C., Umile, T.P., Kieber, D.J., 2005. Biological consumption of
867 carbon monoxide in Delaware Bay, NW Atlantic and Beaufort Sea. *Mar. Ecol.*
868 *Prog. Seri.* 290, 1–14. doi: 10.3354/meps290001

869 Xie, H.X., Bélanger, S., 2009. Photobiogeochemical cycling of carbon monoxide in the
870 southeastern Beaufort Sea in spring and autumn. *Limnol. Oceanogr.* 54(1), 234–
871 249. doi: 10.4319/lo.2009.54.1.0234

872 Xu, G.B., Xu, F., Ji, X., Zhang, J., Yan., S.B., Mao, S.H., Yang, G.P., 2023. Carbon
873 monoxide cycling in the Eastern Indian Ocean. *J. Geophys. Res. Oceans* 128(5).
874 doi: 10.1029/2022JC019411

875 Yamashita, Y., Hashihama, F., Saito, H., Fukuda, H., Ogawa, H., 2017. Factors
876 controlling the geographical distribution of fluorescent dissolved organic matter
877 in the surface waters of the Pacific Ocean. *Limnol. Oceanogr.* 62(6), 2360–2374.
878 doi: 10.1002/lno.10570

879 Yamashita, Y., Jaffé, R., 2008. Characterizing the interactions between trace metals and
880 dissolved organic matter using excitation-emission matrix and parallel factor
881 analysis. *Environ. Sci. Technol.* 42(19), 7374–7379. doi: 10.1021/es801357h

882 Yang, G.P., Watanabe, S., Tsunogai, S., 2001. Distribution and cycling of
883 dimethylsulfide in surface microlayer and subsurface seawater. *Mar. Chem.* 76(3),
884 137–153. doi: 10.1016/S0304-4203(01)00054-8

885 Yang, G.P., Ren, C.Y., Lu, X.L., Liu, C.Y., Ding, H.B., 2011. Distribution, flux, and
886 photoproduction of carbon monoxide in the East China Sea and Yellow Sea in
887 spring. *J. Geophys. Res.: Oceans* 116(C2), C02001. doi: 10.1029/2010jc006300

888 Yang, G.P., Wang, W.L., Lu, X.L., Ren, C.Y., 2010. Distribution, flux and biological
889 consumption of carbon monoxide in the Southern Yellow Sea and the East China
890 Sea. *Mar. Chem.* 122(1–4), 74–82. doi: 10.1016/j.marchem.2010.08.001

891 Yang, L., Zhang, J., Yang, G.P., 2021. Mixing behavior, biological and photolytic
892 degradation of dissolved organic matter in the East China Sea and the Yellow Sea.
893 *Sci. Total Environ.* 762(6), 143164. doi: 10.1016/j.scitotenv.2020.143164

894 Yang, L., Zhang, J., Engel, A., Yang, G.P., 2022. Spatio-temporal distribution,
895 photoreactivity and environmental control of dissolved organic matter in the sea-

896 surface microlayer of the eastern marginal seas of China. *Biogeosciences* 19,
897 5251–5268. doi: 10.5194/bg-19-5251-2022

898 Yang, L., Gong, C.Y., Mo, X.J., Zhang, J., Yang, B., Yang, G.P., 2024. Carbon
899 monoxide in the marine atmosphere and seawater: Spatiotemporal distribution and
900 photobiogeochemical cycling. *J. Geophys. Res.: Oceans* 129(8), e2024JC021286.
901 doi: 10.1029/2024JC021286

902 Yu, C., Lu, C., Li, Y., Li, H., Lin, J., Chang, L., 2025. Spatial and temporal variation
903 of nutrient distribution in the Yangtze River estuary and adjacent waters: insights
904 from GOCI data analysis. *Mar. Environ. Res.* 204. doi:
905 10.1016/j.marenvres.2024.106895

906 Zafiriou, O.C., Andrews, S.S., Wang, W., 2003. Concordant estimates of oceanic
907 carbon monoxide source and sink processes in the Pacific yield a balanced global
908 “blue-water” CO budget. *Global Biogeochem. Cy.* 17(1), 1015–1027. doi:
909 10.1029/2001gb001638

910 Zafiriou, O.C., Xie, H., Nelson, N.B., Wang, N.W., 2008. Diel carbon monoxide
911 cycling in the upper Sargasso Sea near Bermuda at the onset of spring and in
912 midsummer. *Limnol. Oceanogr.* 53(2), 835–850. doi: 10.2307/40006463

913 Zhang, J., Liu, S.M., Ren, J.L., Wu, Y., Zhang, G.L., 2007. Nutrient gradients from the
914 eutrophic Changjiang (Yangtze River) estuary to the oligotrophic kuroshio waters
915 and re-evaluation of budgets for the east China sea shelf. *Prog. Oceanog.* 74(4),
916 449–478.

917 Zhang, J., Wang, J., Zhuang, G.C., Yang, G.P., 2019. Carbon monoxide cycle in the
918 Bohai Sea and the Yellow Sea: Spatial variability, sea-air exchange and biological
919 consumption in autumn. *J. Geophys. Res.: Oceans* 124, 4248–4257. doi:
920 10.1029/2018JC014864

921 Zhang, Y., Xie, H., 2012. The sources and sinks of carbon monoxide in the St.
922 Lawrence system. *Deep-Sea Res. Part II: Topical Studies in Oceanography* 81,
923 114–123. doi: 10.1016/j.dsr2.2011.09.003

924 Zhang, Y., Xie, H., Chen, G., 2006. Factors affecting the efficiency of carbon monoxide
925 photoproduction in the St. Lawrence estuarine system (Canada). *Environ. Sci.*
926 *Technol.* 40(24), 7771–7777. doi: 10.1021/es0615268

927 Zhang, Y., Xie, H., Fichot, C.G., Chen, G., 2008. Dark production of carbon monoxide
928 (CO) from dissolved organic matter in the St. Lawrence estuarine system:
929 Implication for the global coastal and blue water CO budgets. *J. Geophys. Res.:*
930 *Oceans* 113(12), 1–9. doi: 10.1029/2008JC004811

931 Zhu, W.Z., Zhang, H.H., Zhang, J., Yang, G.P., 2018. Seasonal variation in
932 chromophoric dissolved organic matter and relationships among fluorescent
933 components, absorption coefficients, and dissolved organic carbon in the Bohai
934 Sea, the Yellow Sea and the East China Sea. *J. Mar. Syst.* 180, 9–23. doi:
935 10.1016/j.jmarsys.2017.12.003

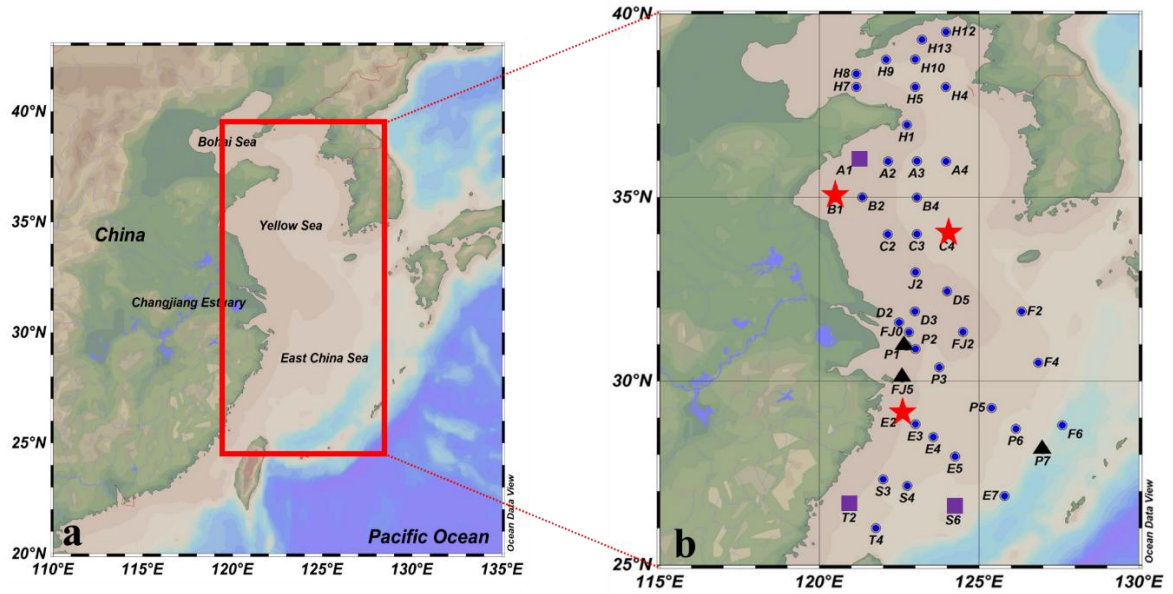
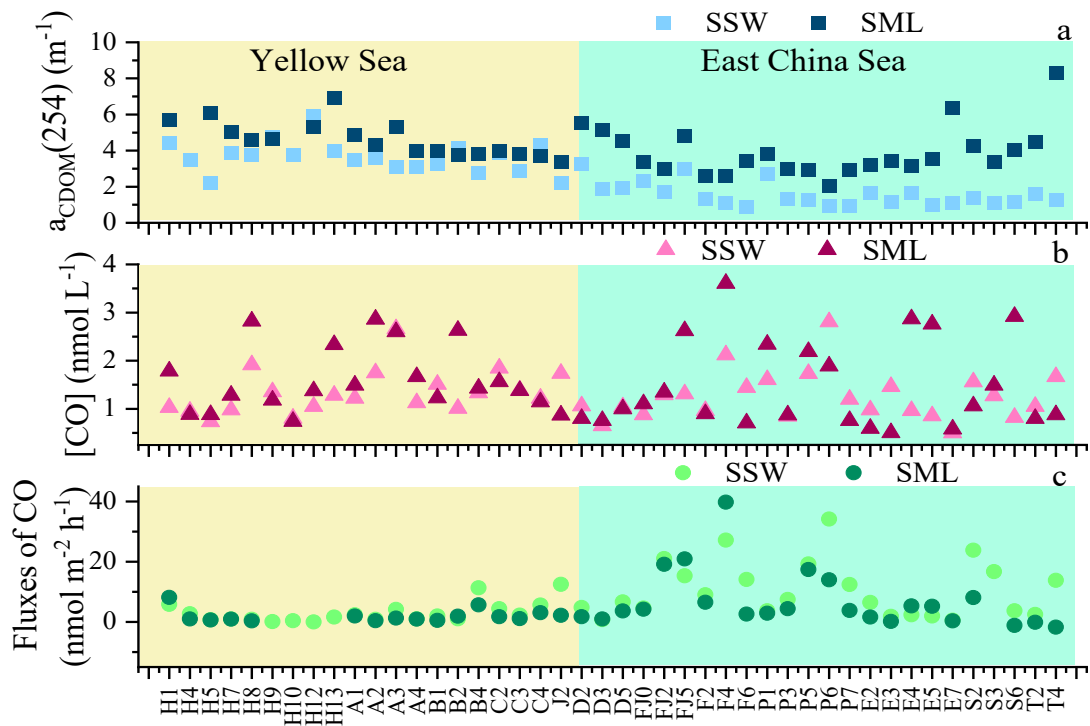
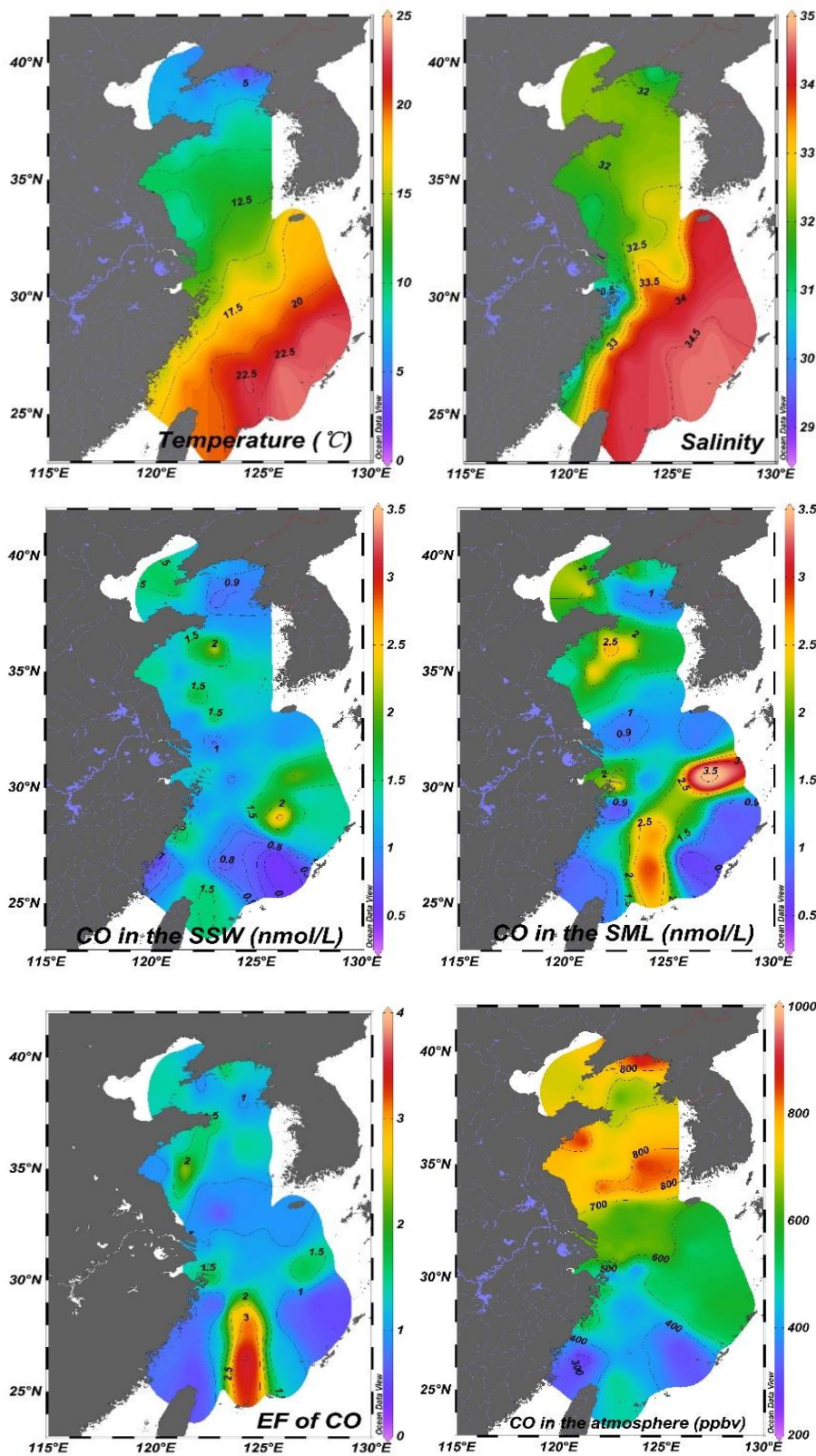


Fig. 1. Map of sampling stations in the East China Sea and the Yellow Sea during winter. Red box represented photochemical incubation experiment stations, and the purple rhomboid represented biological consumption experiment stations.

■ : Stations for CO microbial consumption incubation experiments; ▲ : Stations for CO photochemical production incubation experiments; ★ : Station for both CO microbial consumption and photochemical production incubation experiments; ● : Stations only for seawater sampling.



d



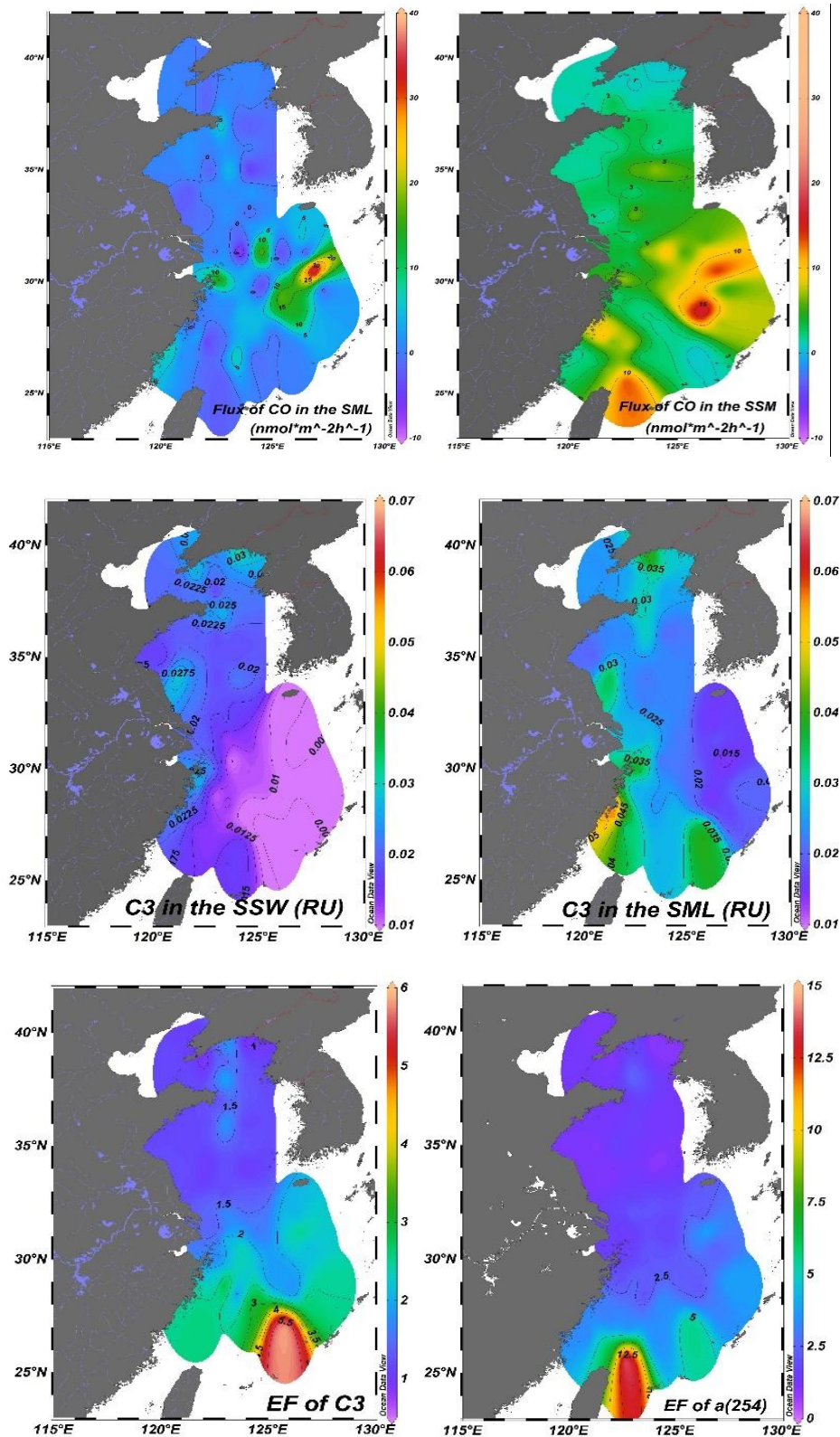


Fig. 2. $a_{\text{CDOM}}(254)$ values in the SSW and the SML (a); CO concentrations in the SSW and the SML (b); The flux of CO in the SSW and the SML (c); Spatial distributions of temperature and salinity, CO and the marine-like fluorescence C3 in the SSW and the SML; CO in the atmosphere, and the enrichment factors of CO and the marine-like fluorescence C3 in the SML in the East China Sea

and the Yellow Sea in January 2020 (d). The concentration profiles of CO in the SSW resemble those of CO in the SML, which is evidence for a biogeochemically very stable environment.

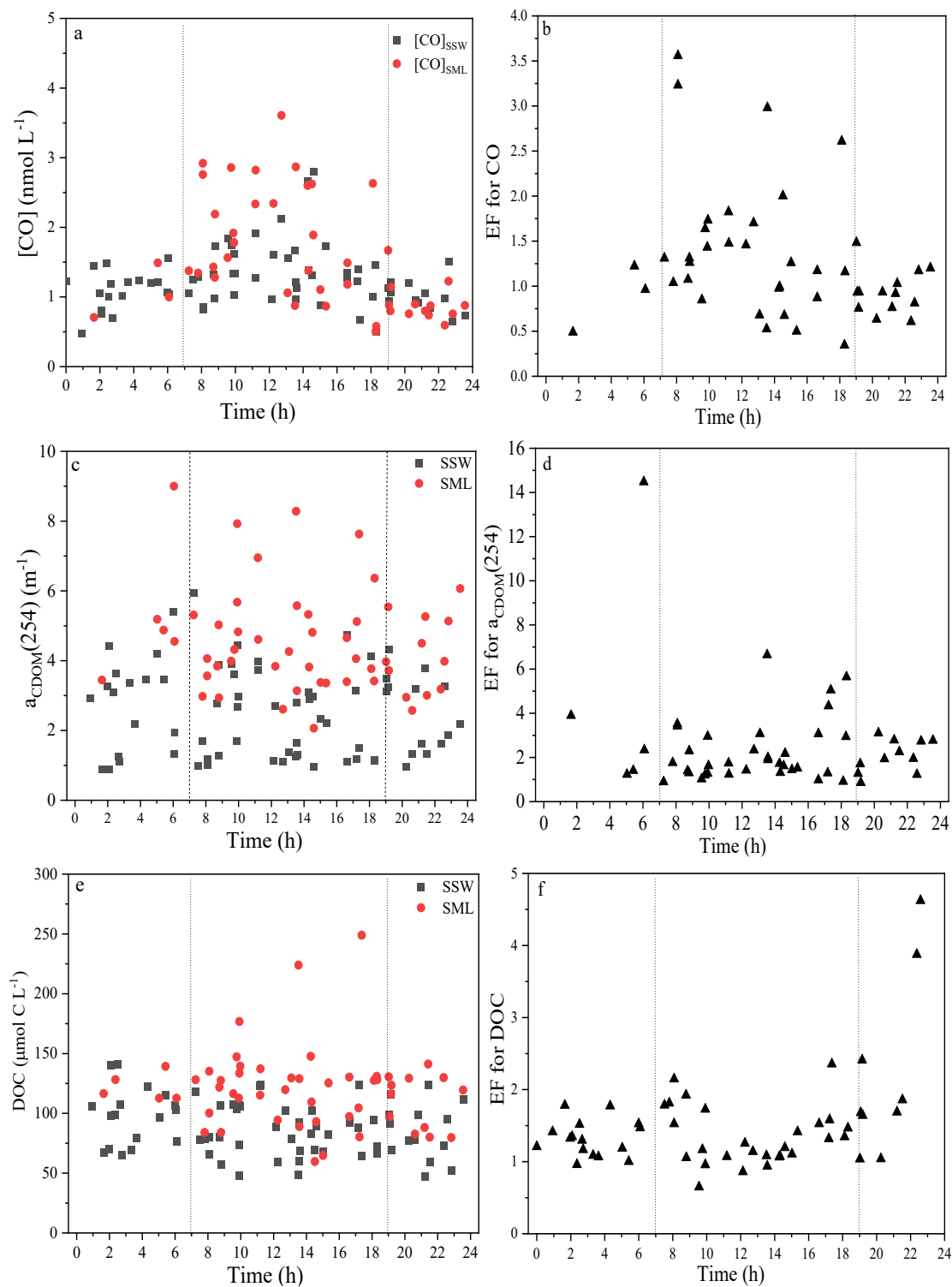


Fig. 3. Variations in the [CO]_{SML}, [CO]_{SSW}, a_{CDOM}(254), and DOC, EFs of [CO], a_{CDOM}(254), and DOC with the sampling time at each station.

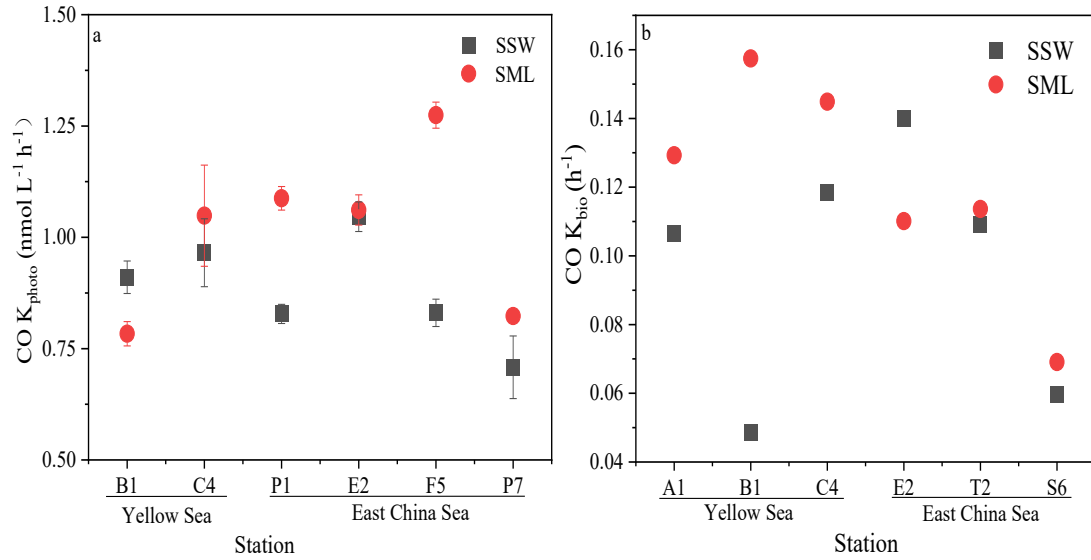
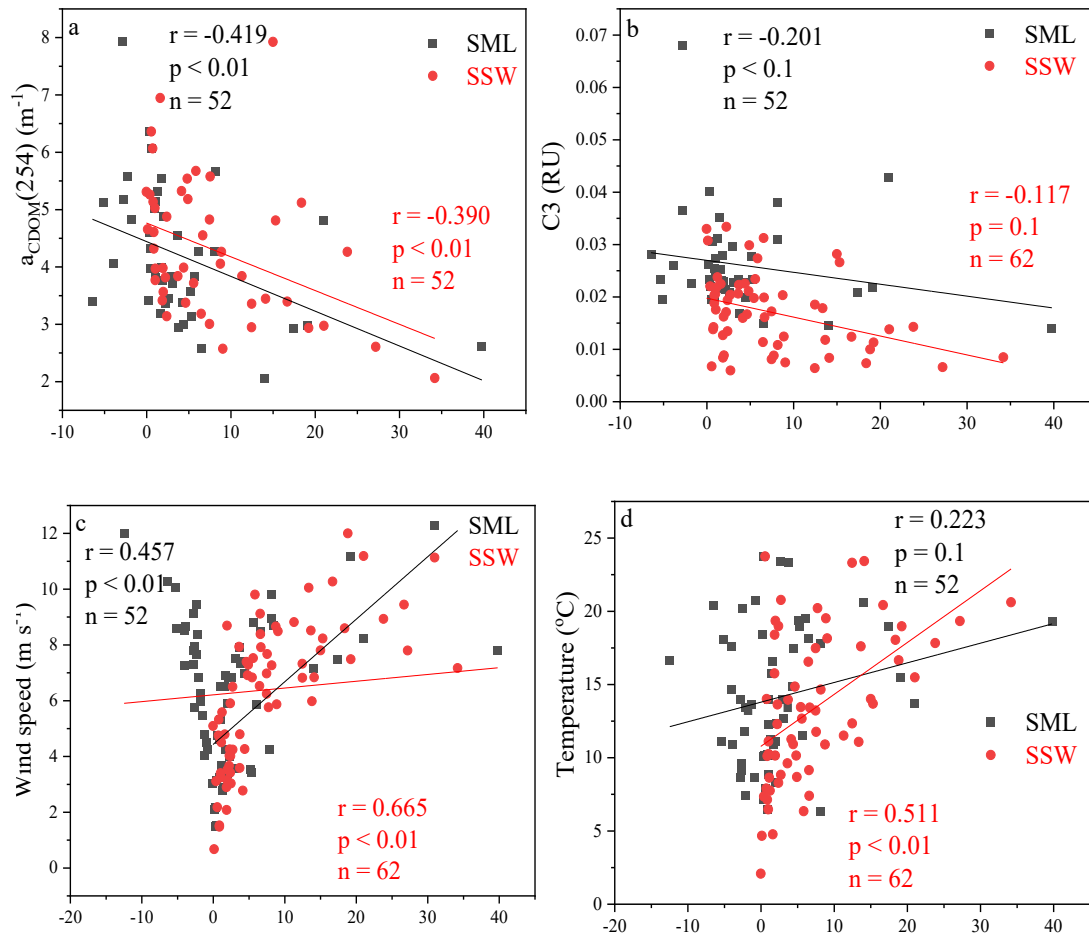


Fig. 4. Variations in photochemical CO production rate of CO (K_{photo}) in the SML (red) and the SSW (black) (a). Variations in microbial consumption rate constants of CO (K_{bio}) in the SML (red) and the SSW (black). Data are presented as mean values and error bars represent the standard deviation of duplicate samples.



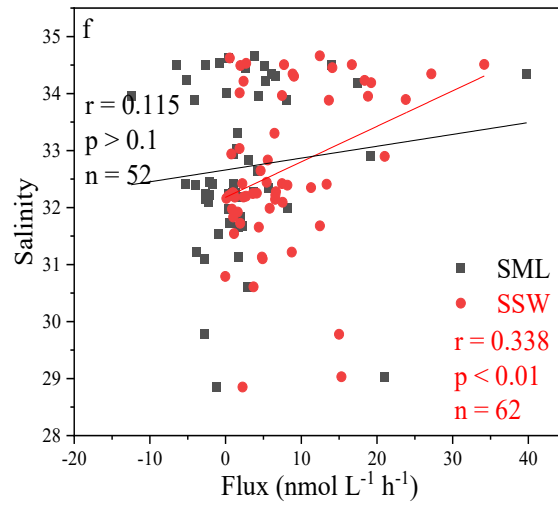


Fig. 5. Correlations between the instantaneous sea-to-air fluxes of CO (Flux) in the SSW and the SML with $a_{\text{CDOM}}(254)$, marine humic-like C3, wind speeds, temperature, and salinity in the East China Sea and the Yellow Sea during winter.

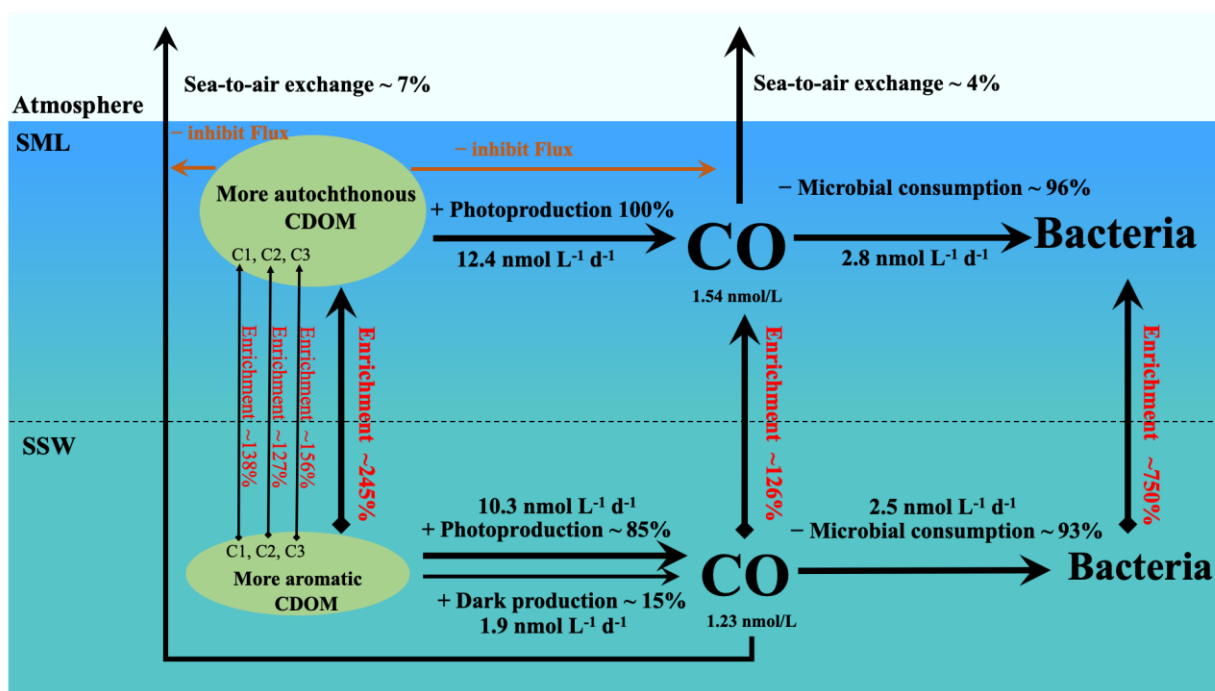


Fig. 6. Budget model of CO transformation in the SML and the SSW in the eastern marginal seas of China during winter. (Bacterial enrichment was calculated by Sun et al., 2020).

Table 1 Correlation coefficients between [CO], CDOM optical parameters, DOC, Chl-*a*, O₂, salinity, and temperature in SSW a) and SML b).

a)

	[CO] _{SSW}	Temperature	Salinity	O ₂	a _{CDOM} (254)	a _{CDOM} (330)	a _{CDOM} (355)	C1	C2	C3	DOC	Chl- <i>a</i>	SUVA ₂₅₄	S ₂₇₅₋₂₉₅	S ₃₅₀₋₄₀₀
Temperature	-0.001														
Salinity	0.017	0.699**													
O ₂	-0.072	-0.977**	-0.723**												
a _{CDOM} (254)	-0.029	-0.907**	-0.716**	0.876**											
a _{CDOM} (330)	-0.118	-0.783**	-0.690**	0.758**	0.939**										
a _{CDOM} (355)	-0.151	-0.717**	-0.622**	0.690**	0.894**	0.990**									
C1	0.008	-0.591**	-0.758**	0.596**	0.675**	0.680**	0.632**								
C2	0.053	-0.324*	-0.341**	0.286*	0.533**	0.592**	0.599**	0.759**							
C3	-0.049	-0.788**	-0.851**	0.779**	0.894**	0.887**	0.838**	0.891**	0.665**						
DOC	0.008	-0.598**	-0.239	0.583**	0.532**	0.394**	0.354**	0.241	0.146	0.323*					
Chl- <i>a</i>	0.109	-0.357**	-0.092	0.415**	0.333**	0.235	0.208	0.104	0.159	0.215	0.348**				
SUVA ₂₅₄	-0.081	-0.676**	-0.705**	0.654**	0.824**	0.860**	0.831**	0.653**	0.560**	0.853**	-0.006	0.134			
S ₂₇₅₋₂₉₅	0.045	0.100	0.099	-0.092	-0.204	-0.385**	-0.448**	-0.197	-0.241	-0.269*	-0.009	0.084	-0.241		
S ₃₅₀₋₄₀₀	-0.001	0.009	-0.060	0.044	-0.095	-0.214	-0.279*	0.009	-0.103	-0.043	-0.088	0.026	-0.050	0.867**	
S _R	0.059	0.346**	0.421**	-0.429**	-0.254*	-0.220	-0.134	-0.343**	-0.104	-0.393**	-0.087	-0.148	-0.316*	-0.506**	-0.645**

*Correlation is significant at the 0.05 level (two-tailed).

**Correlation is significant at the 0.01 level (two-tailed). N = 44.

b)

	[CO] _{smi}	Temperature	Salinity	SML a _{CDOM} (254)	SML a _{CDOM} (330)	SML a _{CDOM} (355)	SML C1	SML C2	SML C3	SML DOC	SML SUVA ₂₅₄	SML S ₂₇₅₋₂₉₅	SML S ₃₅₀₋₄₀₀
Temperature	-0.032												
Salinity	-0.098	0.699**											
SML a _{CDOM} (254)	-0.137	-0.037	-0.045										
SML a _{CDOM} (330)	-0.119	-0.113	-0.135	0.948**									
SML a _{CDOM} (355)	-0.143	-0.114	-0.146	0.901**	0.989**								
SML C1	-0.095	0.158	-0.156	0.711**	0.504**	0.434**							
SML C2	-0.217	0.089	-0.106	0.670**	0.675**	0.673**	0.702**						
SML C3	-0.060	0.092	-0.154	0.823**	0.622**	0.541**	0.938**	0.703**					
SML DOC	-0.018	0.136	0.174	0.898**	0.783**	0.705**	0.572**	0.280	0.665**				
SML SUVA ₂₅₄	-0.063	-0.250	-0.439**	0.136	0.303*	0.376**	0.240	0.501**	0.262	-0.272			
SML S ₂₇₅₋₂₉₅	0.254	0.241	0.223	0.040	-0.217	-0.318*	0.323*	-0.056	0.336*	0.216	-0.409**		
SML S ₃₅₀₋₄₀₀	0.270	0.112	0.082	0.136	-0.090	-0.187	0.385**	0.047	0.427**	0.244	-0.281	0.968**	
SML S _R	-0.288	0.231	0.213	-0.248	-0.057	0.044	-0.276	0.029	-0.339*	-0.296*	0.167	-0.726**	-0.776**

*Correlation is significant at the 0.05 level (two-tailed).

**Correlation is significant at the 0.01 level (two-tailed). N = 44.

Table 2 Correlation coefficients between EFs of CO, DOM absorption, DOC, three fluorescence components, temperature, salinity, and wind speed.

	EF of CO	EF of DOC	EF of a _{CDOM} (254)	EF of a _{CDOM} (330)	EF of a _{CDOM} (355)	EF of C1	EF of C2	EF of C3	Temperature	Salinity	Wind speed
EF of DOC	-0.098										
EF of a _{CDOM} (254)	-0.067	0.867**									
EF of a _{CDOM} (330)	-0.111	0.726**	0.912**								
EF of a _{CDOM} (355)	-0.124	0.556**	0.752**	0.945**							
EF of C1	0.081	0.731**	0.898**	0.753**	0.619**						
EF of C2	-0.084	0.149	0.586**	0.600**	0.580**	0.486**					
EF of C3	-0.022	0.796**	0.935**	0.830**	0.714**	0.964**	0.502**				
Temperature	0.037	0.363**	0.528**	0.533**	0.456**	0.617**	0.296*	0.604**			
Salinity	0.006	0.289*	0.478**	0.493**	0.427**	0.500**	0.268	0.491**	0.699**		
Wind speed	-0.177	0.008	0.186	0.159	0.161	-0.130	-0.006	-0.105	0.129	0.052	
Solar irradiance	0.409**	-0.024	-0.051	-0.082	-0.050	0.022	-0.139	0.002	0.160	0.157	0.104

*Correlation is significant at the 0.05 level (two-tailed).

**Correlation is significant at the 0.01 level (two-tailed). N = 44.